

## RESEARCH ARTICLE

10.1029/2018JE005550

## Special Section:

Mars Aeronomy

## Key Points:

- A high altitude polar warming feature is observed at intermediate northern latitudes near perihelion
- Heating and cooling above and below 150 km, respectively, is observed that coincides with 27-day solar EUV variability
- The mean temperature sensitivity to EUV forcing is found to be  $45 \pm 12 \text{ K}\cdot\text{m}^2\cdot\text{mW}^{-1}$  at the terminator, independent of dawn or dusk location

## Correspondence to:

E. M. B. Thiemann,  
thiemann@asp.colorado.edu

## Citation:

Thiemann, E. M. B., Eparvier, F. G., Bougher, S. W., Dominique, M., Andersson, L., Girazian, Z., et al. (2018). Mars thermospheric variability revealed by MAVEN EUVM solar occultations: Structure at aphelion and perihelion and response to EUV forcing. *Journal of Geophysical Research: Planets*, 123. <https://doi.org/10.1029/2018JE005550>

Received 24 JAN 2018

Accepted 1 AUG 2018

Accepted article online 15 AUG 2018

## Mars Thermospheric Variability Revealed by MAVEN EUVM Solar Occultations: Structure at Aphelion and Perihelion and Response to EUV Forcing

E. M. B. Thiemann<sup>1</sup> , F. G. Eparvier<sup>1</sup> , S. W. Bougher<sup>2</sup> , M. Dominique<sup>3</sup> , L. Andersson<sup>1</sup> , Z. Girazian<sup>4</sup> , M. D. Pilinski<sup>1</sup> , B. Templeman<sup>1</sup>, and B. M. Jakosky<sup>1</sup> 

<sup>1</sup>Laboratory for Atmospheric and Space Physics, University of Colorado, Boulder, CO, USA, <sup>2</sup>Climate and Space Sciences and Engineering, University of Michigan, Ann Arbor, MI, USA, <sup>3</sup>Royal Observatory of Belgium, Uccle, Belgium, <sup>4</sup>NASA Goddard Space Flight Center, Greenbelt, MD, USA

**Abstract** The Mars thermosphere holds clues to the evolution of the Martian climate and has practical implications for spacecraft visiting Mars, which often use it for aerobraking upon arrival, or for landers, which must pass through it. Nevertheless, it has been sparsely characterized, even when past accelerometer measurements and remote observations are taken into account. The Mars Atmosphere and Volatile Evolution (MAVEN) orbiter, which includes a number of instruments designed to characterize the thermosphere, has greatly expanded the available thermospheric observations. This paper presents new and unanticipated measurements of density and temperature profiles (120–200 km) derived from solar occultations using the MAVEN Extreme Ultraviolet (EUV) Monitor (EUVM). These new measurements complement and expand MAVEN's intended thermospheric measurement capacity. In particular, because the local time is inherently fixed to the terminator, solar occultations are ideally suited for characterizing long-term and latitudinal variability. Occultation measurements are made during approximately half of all orbits, resulting in thousands of new thermospheric profiles. The density retrieval method is presented in detail, including an uncertainty analysis. Altitude-latitude maps of thermospheric density and temperature at perihelion and aphelion are presented, revealing structures that have not been previously observed. Tracers of atmospheric dynamics are also observed, including (1) a high altitude polar warming feature at intermediate latitudes, (2) cooler temperatures coinciding with increased gravity wave activity, and (3) an apparent thermostatic response to solar EUV heating during a solar rotation, which shows heating at high altitudes that is accompanied by cooling at lower altitudes.

**Plain Language Summary** Solar extreme ultraviolet (EUV) radiation is the primary energy source for the thermosphere, the uppermost region of the Mars atmosphere. The Mars Atmosphere and Volatile Evolution (MAVEN) orbiter is equipped with the EUV Monitor (EUVM) to track how this region of the spectrum varies. Because EUV radiation is entirely absorbed in the thermosphere, it can be used to probe this region of the atmosphere when the Sun sets or rises over the horizon as viewed from MAVEN using the solar occultation technique. This study presents new temperature and density measurements of the Mars thermosphere made by EUVM solar occultations, which include the first observations of both expected and unexpected phenomena. This includes a warming trend at intermediate altitudes in the winter hemisphere and a cooling trend in the lower thermosphere in response to a relatively rapid increase in solar EUV radiation. These results will aid our understanding of how the Mars upper atmosphere has evolved over time and, in particular, how significant fractions of the atmosphere have been lost to space. Further, these results provide valuable data for mission planners to aid in orbit determination and entry into the atmosphere by landers, both manned or unmanned.

### 1. Introduction

The Mars thermosphere (~100–200 km) couples the atmosphere with the near-space environment. It begins at the top of the well-mixed atmosphere at the temperature minimum known as the mesopause. In the vicinity of the mesopause also lies the homopause, where atmospheric species tend to diffusively separate according to mass (Bougher, Brain et al., 2017). This results in (heavier) CO<sub>2</sub> being the dominant species below approximately 200–220 km and (lighter) atomic O being the dominant species above 200–220 km (Bougher, Jakosky, et al., 2015; Mahaffy, Benna, Elrod, et al., 2015; Nier & McElroy, 1977). Near 170–200 km

lies the exobase, in the vicinity of which collisions become rare. Above the exobase, atmospheric kinematics becomes less fluid-like and more particle-like, and the thermosphere blends into the exosphere, with no strict delineation between the two.

Solar extreme ultraviolet (EUV, 10–121 nm) radiation is the primary energy input to the thermosphere, with the majority of EUV irradiance being absorbed between 100 and 220 km and the absorption peak occurring near 130 km. This results in a solar cycle dependence on thermospheric temperature, causing it to range from approximately 150 to 350 K from solar minimum to maximum at the exobase (Bougher, Pawlowski, et al., 2015; González-Galindo et al., 2015). In addition to EUV radiation, other factors, including energy transport from global circulation and upward propagating atmospheric waves, contribute to the thermospheric thermal balance (Bougher et al., 2000, 2009; Medvedev et al., 2011, 2015). These factors can result in seemingly random fluctuations in thermospheric temperature and density, as can occur from gravity waves (e.g., Yiğit, England, et al., 2015) or quasi-periodic fluctuations as can occur from atmospheric tides (e.g., Liu et al., 2017; Lo et al., 2015), or more gradual variations as can occur from large-scale circulation patterns occurring in the Mars upper atmosphere (e.g., Bougher et al., 2006). CO<sub>2</sub> 15- $\mu$ m radiative cooling is significant in the lower thermosphere, near the EUV absorption peak, but is believed to be a secondary cooling mechanism, locally, in the middle and upper thermosphere (Bougher et al., 1999; Medvedev et al., 2015).

Understanding the variability in the thermosphere's structure is important for characterizing global circulation, quantifying atmospheric escape and ultimately understanding the evolution of Mars's climate. More directly, the Martian thermosphere impacts spacecraft during their aero-braking campaigns, where atmospheric drag is used to dump momentum for orbit adjustment. For these reasons, the thermosphere has been characterized by a number of probes that have visited the red planet, beginning with remote measurements made by the first Mariner fly-by in 1965 (Fjeldbo et al., 1966), later by the Viking landers' in situ measurements (Nier & McElroy, 1977) as well as during the aero-braking campaigns of the Mars Odyssey, Mars Global Surveyor and Mars Reconnaissance Orbiter missions (Bougher, Brain, et al., 2017; Keating et al., 1998; Withers, 2006), and most recently by the Mars Atmosphere and Volatile Evolution (MAVEN) mission (e.g., Bougher, Jakosky, et al., 2015; Elrod et al., 2017; Evans et al., 2015; Jain et al., 2015; Mahaffy, Benna, Elrod, et al., 2015; Zurek et al., 2017). Nevertheless, the Martian thermosphere is still poorly understood, and observations of its variability continue to provide new insight into the processes occurring in the Mars atmosphere. Understanding this variability and how it relates to the evolution of the Martian climate are one of the goals of MAVEN.

MAVEN is tasked with characterizing how the upper atmosphere of Mars varies in the current epoch in order to better understand how the atmosphere has evolved over time and does so with a set of instruments that both characterize the solar drivers and the planet's response to these drivers (Jakosky et al., 2015). MAVEN is able to characterize Mars's near-space environment and upper atmosphere with a highly elliptical 150  $\times$  6,000-km, 4.5-hr orbit, which allows MAVEN to make in situ measurements of both the solar wind and upper atmosphere in the same orbit. The MAVEN orbit precesses such that the in situ measurements span a wide range of local times and latitudes in the atmosphere, in addition to the major regions of the near-space environment (e.g., solar wind, bow-shock, and magnetosheath). MAVEN began science operations in November 2014 and has continued to operate nominally through the time of this writing. The current MAVEN mission spans over 1.5 Mars years (MY), during which the solar cycle declined from moderate to minimum activity conditions (Lee et al., 2017).

MAVEN includes three instruments that are designed to characterize thermospheric density: The Accelerometer (ACC; Zurek et al., 2015), the Neutral Gas and Ion Mass Spectrometer (NGIMS; Mahaffy, Benna, King, et al., 2015), and the Imaging Ultraviolet Spectrograph (IUVS; McClintock et al., 2015). ACC and NGIMS make routine in situ density measurements near periapsis, with typical reliable measurement sensitivity between 145 and 250 km for NGIMS and between 145 and 170 km for ACC. Note that the ACC and NGIMS minimum measurement altitudes are lowered to near 120–130 km during periodic "Deep Dip" Campaigns (Bougher, Jakosky, et al., 2015; Zurek et al., 2017), corresponding to a periapsis density corridor that is raised to approximately 2–3.5 kg/km<sup>3</sup> for 1-week intervals. These campaigns have occurred at a cadence of approximately once every 3 months. IUVS measures thermospheric density remotely through routine limb scan measurements of atmospheric airglow (Evans et al., 2015; Jain et al., 2015). These observations are made with multiple scans during the periapsis orbit segment, observing locations ranging from

approximately 100 to 1,000 km perpendicularly away from the orbit track, with a reliable measurement sensitivity between 120- and 180-km altitude. Additionally, IUVS measures thermospheric density during special stellar occultation campaigns (Gröller et al., 2015, 2018), occurring approximately every 2 months. The IUVS stellar occultation observations measure atmospheric density from near the surface to 150 km.

This paper presents new thermospheric density measurements between 120 and 200 km, retrieved from solar occultation measurements made by the MAVEN EUV Monitor (EUVM; Eparvier et al., 2015). The primary purpose of MAVEN EUVM is to characterize solar EUV irradiance at Mars. This paper demonstrates that thermospheric densities can be accurately inferred from the extinction of the solar signal measured by EUVM as the spacecraft enters or exits eclipse since EUV radiation is absorbed entirely in the thermosphere. Because solar occultations are inherently confined to the terminator, the EUVM solar occultations (EUVM-SOs) are generally not collocated with those made by the other MAVEN instruments, broadening the global coverage of neutral density measurements made by MAVEN during a single orbit. Furthermore, the fact that the local time (LT, not to be confused with *Local Solar Time*, which depends on the solar declination angle and varies at the terminator with latitude) is fixed to either 06:00 (at the dawn terminator) or 18:00 (at the dusk terminator) make EUVM-SOs more suitable for characterizing long-term or latitudinal variability than the other MAVEN neutral density instruments, which must contend with varying LT and/or solar zenith angle. This paper begins by describing the method used to retrieve density from the EUVM-SOs. The data used in the density retrievals are then presented, followed by the estimated uncertainty associated with the density retrievals. Next, results of the density profiles made during the MAVEN mission to-date are presented. These results include altitude-latitude maps of density and temperature, as well as an analysis of how thermospheric temperature varies with solar EUV irradiance and season. These results are discussed and put into the context of our current understanding of the Mars atmosphere and existing global model simulations.

## 2. Methods

### 2.1. Retrieving Neutral Density From EUVM Solar Occultations

Retrievals from the EUVM-SO measurements use full-disk integrated observations of the Sun in the 17–22-nm range. Therefore, they are complicated by the spatial extent of the Sun, spanning ~25–35 km at Mars's limb as viewed from MAVEN, which is larger than multiple thermospheric scale heights. Additionally, at EUV wavelengths, the radiance is highly variable over the solar disk, being brighter over solar active regions and dimmer over coronal holes. Roble and Norton (1972) devised a technique that uses reference atmospheres to account for the extinction of the spatially extended solar disk through the atmosphere. Thiemann, Dominique, et al. (2017) expanded this method by incorporating solar EUV images into the retrieval. The methods of Roble and Norton (1972) and Thiemann, Dominique, et al. (2017) are used to retrieve thermospheric neutral density from the EUVM-SO measurements. A brief description of the retrieval method is summarized here, but the reader is referred to those two papers for a detailed description of the retrieval method. In particular, the study of Thiemann, Dominique, et al. (2017) was motivated by an effort to validate methods used in this study by applying them at the Earth, where thermospheric densities are better understood. As such, the method of Thiemann, Dominique, et al. (2017) is nearly identical to the method used in this study. Deviations between the methods used here and those by Thiemann, Dominique, et al. (2017) are specified as they arise.

The fundamental solar occultation measurement quantity is the Extinction Ratio (ER), which relates the observed solar intensity,  $I$ , at tangent height,  $h_t$ , to that at the top of the atmosphere ( $I_\infty$ ) according to

$$\text{ER} = \frac{I(h_t)}{I_\infty} = \exp(-\sum_i N_i(h_t)\sigma_i), \quad (1)$$

where  $N_i(h_t)$ ,  $\sigma_i$ , and  $h_t$  are the column density along the line-of-sight, the absorption cross section of the  $i$ th absorbing species, and the height above the surface tangent to the line of sight, respectively. Equation (1) is forward modeled to find the altitude profile of  $N_i$  that results in a predicted ER in closest agreement with the measured ER. The solar intensities, atmospheric cross sections, and instrument response function used in the forward model are at 0.1-nm resolution and described in detail in section 3.

To account for the finite extent of the Sun, solar images and reference atmospheres are incorporated into the retrieval algorithm. Signal extinction is forward modeled by integrating the intensity of the solar disk

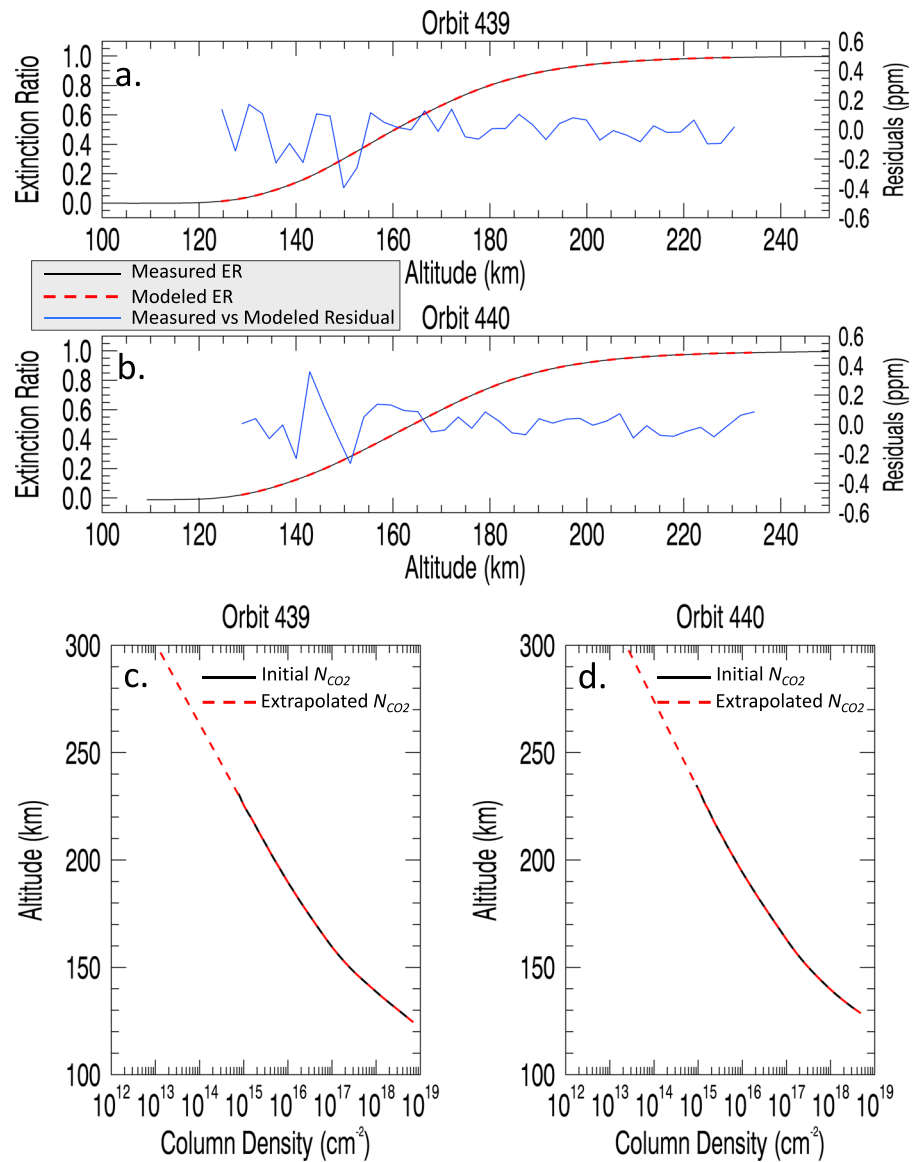


**Figure 1.** Panels (a) and (b) show sample extinction ratios from the MAVEN Extreme Ultraviolet Monitor 17–22-nm channel with black curves. The resulting Extinction Ratio (ER) fits from solving equation (1) are shown with red dashed curves. (c) and (d) show the retrieved column densities and the extrapolated column densities, the latter of which is inverted for number density, with black and red dashed curves, respectively.

propagating through a reference atmosphere when predicting  $N_i$  at a particular  $h_r$ . For a given occultation scan, only the reference atmosphere scale height is fixed, and independent reference atmospheres are computed for each ER value within a scan. The process is iterated until the scale height between 150 and 180 km of the reference and retrieved atmospheres agree to within 5%, which is the approximate measurement random uncertainty and described in further detail in section 4. In practice, the mean absolute difference between the reference and the retrieved scale height is 2.2%. Figure 1 in Thiemann, Dominique, et al. (2017) and the associated text illustrate an example of this method for solar occultations at Earth.

The retrievals presented here assume a pure CO<sub>2</sub> atmosphere, allowing the summation in equation (1) to reduce to  $N_{\text{CO}_2}\sigma_{\text{CO}_2}$ . This assumption is justified for the following reasons: There typically is minimal extinction of the EUVM signal at altitudes where O becomes the major species. Further, the CO<sub>2</sub> cross section is three to five times larger than that of O in the 17–22-nm wavelength range, where EUVM-SO

measurements are made. As such, at 200 km, where the O to CO<sub>2</sub> ratio is close to 0.25 (e.g., Bougher, Jakosky, et al., 2015), the contribution of O to the observed extinction is less than 10%. Nevertheless, neglecting O introduces measurable error at high altitudes, and evidence of O contaminating the retrieved density profiles is evident in some cases. Therefore, caution is needed when analyzing data at or above 200 km, and any scale-height increases at these altitudes should be treated with suspicion because the observed temperature is expected to be constant above approximately 170 km, where atmospheric collisions become negligible. Additionally, O contamination may be more prevalent at the Dawn terminator, where thermospheric winds create an O bulge (e.g., Bougher et al., 1999, 2000; Bougher, Pawlowski, et al., 2015), but the EUVM-SO data have not been systematically analyzed in this regard. This assumption of a pure CO<sub>2</sub> atmosphere is accounted for in the uncertainty estimates presented in section 4.

Although the Mars upper atmosphere can be approximated as having two scale heights between 100 and 200 km, one corresponding with the colder well-mixed lower atmosphere and the other with the warmer thermosphere, which warms rapidly above the mesopause resulting in an inflection near 120 km on a linear-logarithmic scale, only single scale-height atmospheres are used as the reference atmospheres. The reference atmospheres used in the retrieval are isothermal with the form  $n(z) = n(z_0)\exp((z - z_0)/H)$ , where  $n$ ,  $z$ ,  $z_0$ , and  $H$  are the number density, altitude, reference altitude, and scale height, respectively. Roble and Norton (1972) and Thiemann, Dominique, et al. (2017) showed that isothermal reference atmospheres do not force the retrieved atmospheres to also be isothermal, and temperature gradients are accurately captured at altitudes above an abrupt change in scale height. However, error induced by the reference atmospheres increases markedly with decreasing altitude below an abrupt change in scale height. The error introduced due to using single scale-height reference atmospheres is quantified in the uncertainty estimates presented in section 4.

Once equation (1) has been solved for  $N_{\text{CO}_2}(h_t)$  for every  $h_t$  in a given occultation scan, Abel inversion is used to convert  $N_{\text{CO}_2}(h_t)$  to  $n_{\text{CO}_2}(h_t)$ , the number density at each  $h_t$ . The Abel inversion requires the assumption of spherical symmetry, which is questionable at the terminator. However, this assumption is reasonable when considering that it is required only over the ~400-km column of atmosphere sampled in the retrieval, which corresponds with approximately 6.8° of longitude. Further, Thiemann, Dominique, et al. (2017) compared the Earth measured thermospheric density retrievals with climate model predictions and found no systematic biases due to the spherical symmetry assumption.

Figure 1 shows sample data and fits from orbits 439 and 440, occurring on 21 December 2014, in order to demonstrate the data quality in the intermediate steps of the retrieval process. Figures 1a and 1b show the measured ER with black curves. Note that the typical EUVM measurement noise is 30 ppm (Thiemann, 2016) and neither it nor solar variability is distinguishable in typical ER measurements. The effects of both types of variability on the retrieval uncertainty are discussed in section 4. For each measured ER value,  $N_{\text{CO}_2}$  is found by forward modeling equation (1); this result is shown with the red dashed curves. Because the numerical solver can fail to find solutions at the ER extremes, only ER measurements in the 0.01–0.99 range are used. The fractional model-measurement difference is shown with the blue curve and right-hand axis and is less than 1 ppm. Figures 1c and 1d show the corresponding retrieved  $N_{\text{CO}_2}$  profiles with black curves, which are inverted for number density using an Abel transform. Because the Abel integral extends to infinity, the topside column density is extrapolated to 3,000-km altitude (essentially infinity) by fitting the upper quartile  $N_{\text{CO}_2}$  values to an exponential function and applying the fit results to altitudes above the highest retrieved  $N_{\text{CO}_2}$  value through 3,000 km; this profile is shown with the red dashed curves.

## 2.2. Method for Inferring Temperature From Density Profiles

Once  $n_{\text{CO}_2}(h_t)$  has been retrieved, a corresponding temperature profile,  $T(h_t)$ , is inferred using the method of Snowden et al. (2013). This method infers temperature by first computing pressure,  $p(h_t)$ , at each altitude by integrating

$$p(h_t) = m_{\text{CO}_2} \int_{h_t}^{\infty} n_{\text{CO}_2}(h_t) g(h_t) dz, \quad (2)$$

where  $m_{\text{CO}_2}$  and  $g(h_t)$  are the CO<sub>2</sub> mass and the local acceleration due to gravity, respectively. Once the pressure is found, hydrostatic equilibrium is invoked and  $T(h_t)$  is found from the ideal gas law,

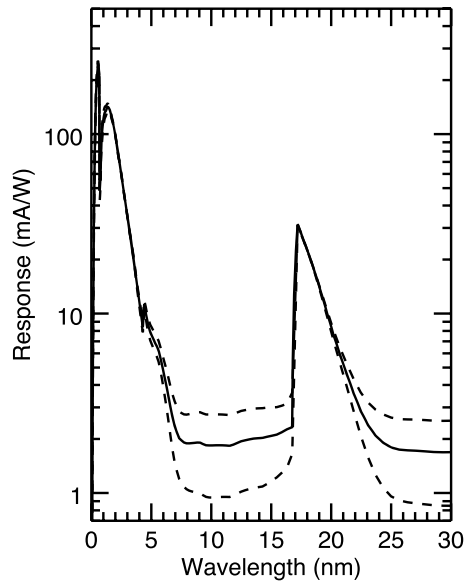


**Figure 2.** The response function (solid curve) and uncertainty (dashed curves) for the Extreme Ultraviolet Monitor Al/Nb/C channel.

$$T(h_t) = \frac{p(h_t)}{n_{\text{CO}_2}(h_t)k}, \quad (3)$$

where  $k$  is the Boltzmann's constant. The method used here differs from that of Snowden et al. (2013) in that in this work,  $n_{\text{CO}_2}(h_t)$  is extrapolated to high altitudes (essentially infinity) whereas Snowden et al. (2013) estimated the absolute pressure at the top of the density profile. Density extrapolation to high altitudes is possible here because the EUVM-SO measurements retrieve density above the exobase, where the atmosphere is approximately isothermal. Isothermality allows for the density profile above the exobase to be approximated by

$$n(h_t > z_{\text{exo}}) \cong n(z_{\text{exo}}) \exp\left(- (h_t - z_{\text{exo}}) \frac{m_{\text{CO}_2}g(h_t)}{kT_{\text{exo}}}\right), \quad (4)$$

where  $z_{\text{exo}}$  is the exobase altitude,  $m_{\text{CO}_2}$  is the  $\text{CO}_2$  molecular mass, and  $T_{\text{exo}}$  is the exospheric temperature.

In practice,  $T_{\text{exo}}$  is found by fitting the measured  $n_{\text{CO}_2}(h_t)$  between  $5 \times 10^7$  and  $2 \times 10^8 \text{ cm}^{-3}$  to equation (4), where the lower density bound corresponds with where the measurement uncertainty becomes large and the upper density bound corresponds with where the mean-free-path of a  $\text{CO}_2$  molecule is approximately equal to a scale height, which is the traditional definition of the exobase. Equation (4) is then used with  $T_{\text{exo}}$  to extend the measured  $n_{\text{CO}_2}(h_t)$  100 km above where  $n_{\text{CO}_2}(h_t) = 5 \times 10^7 \text{ cm}^{-3}$ , which is essentially infinity for the purposes of calculating pressure relative to altitudes where EUVM-SO measurements are made.  $p(h_t)$  is then found by solving equation (2).

### 3. Data Used for Retrieving Density

The EUVM-SO density retrievals require the following data as inputs: EUVM solar measurements, the EUVM instrument response function, a contemporary solar irradiance spectrum,  $\text{CO}_2$  absorption cross sections, and a contemporary solar image. Each of these inputs will be described in this section.

MAVEN EUVM's primary mission is to characterize the solar EUV input into the Mars upper atmosphere and does so using three photometer channels that measure full disk solar EUV irradiance over different wavelength ranges. EUVM uses a simple optical design, with each channel consisting of an entrance aperture, a field-of-view (FOV) limiting aperture, a normal incidence filter, and an AXUV technology (Gullikson et al., 1996) Si detector. The channel band passes are 0.1–7, 0.1–7 + 17–22, and 117–127 nm, determined by an Al/Ti/C foil filter, an Al/Nb/C foil filter, and an Al on  $\text{MgF}_2$  substrate interference filter, respectively. The three band passes were chosen because they originate in distinct regions of the Sun's atmosphere, each with a distinct characteristic variability, providing a diverse set of inputs to the Flare Irradiance Spectral Model-Mars (FISM-M; Thiemann, Chamberlin, et al., 2017), which predicts solar spectral irradiance between 0.1 and 190 nm. The direct irradiance measurements and FISM-M modeled irradiances are reported in the MAVEN EUVM Level 2 and Level 3 data products, respectively, publicly available through the NASA Planetary Data System.

The EUVM-SO densities reported here are from the Al/Nb/C channel of the EUVM instrument, which nominally measures irradiance in the 17–22-nm band but includes a pass band in the 0.1–7-nm range. The fully calibrated irradiances are not used for EUVM-SO measurements because they incorporate a spectral model to isolate and remove the 0.1–7-nm contribution from the measurement, and this contribution must be considered in the EUVM-SO measurements because it contributes to the observed extinction profile. Instead, partially calibrated irradiances are used that have been corrected for dark current, a visible light leak, temperature, gain drifts, and field-of-view effects. These partially calibrated irradiances are stored in the "Corrected Counts" variable of the MAVEN EUVM Level 2 data product.

The response function of an EUVM channel determines which wavelengths of incident radiation contribute to the measured signal and depends on the filter transmission and the responsivity of the detector for each channel. Quantitatively, it is the photocurrent produced per incident optical power as a function of wavelength. Figure 2 shows the modeled response function and uncertainty for the Al/Nb/C channel. The

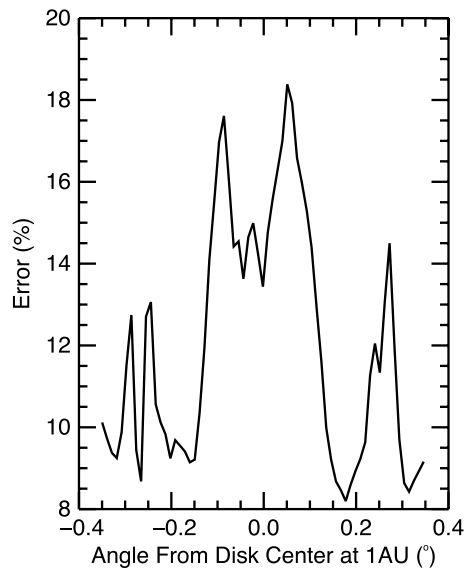


**Figure 3.** Error associated with interpolating extreme ultraviolet images measured at the Earth to Mars. Error is shown as a function of angle along the zenith direction from the Martian surface projected onto the solar disk.

EUVM channel response functions were characterized at the National Institute of Standards and Technology Synchrotron Ultraviolet Radiation Facility (SURF) III (Arp et al., 2000), and detailed results of the characterization are reported in Thiemann (2016). SURF III produces spectra at EUV wavelengths whose intensity and spectrum are strictly constrained by the synchrotron beam-current and energy, both of which are well characterized, resulting in spectral uncertainties smaller than 0.6% at wavelengths above 1 nm (Arp et al., 2000). Multiple beam energies, each with a unique characteristic spectrum, were used to probe each EUVM channel response function, and the detector and filter thicknesses used in the response function model were adjusted until the instrument response (i.e., the ratio of input optical power to output signal) was constant across all beam energies. This method was used by Woods et al. (1999, 2005) to calibrate the soft X-ray and EUV photometers on the X-Ray Photometer System onboard the Solar Radiation and Climate Experiment (SORCE) and the Thermosphere Ionosphere Mesosphere Energetics and Dynamics (TIMED) missions. Thiemann (2016) updated this method to account for defects in the foil filters, termed pinholes, that allow light to pass directly through the foil as the name suggests (Powell, 1993). Thiemann (2016) found that the characterized response function filter and detector thickness are in substantially better agreement with those reported by the manufacturer when pinholes are considered and, therefore,

the response function model that includes pinholes is considered to be the best estimate. Because of the indirect nature of the response function characterization, its associated uncertainty is difficult to quantify. For the purposes of computing the density retrieval uncertainty estimate presented in section 4, the response function uncertainty is conservatively estimated as the difference between the response function model that includes pinholes and the model that does not, divided by  $\sqrt{2}$ .

Daily averaged FISM-M solar spectra are used in the density retrievals. The bin-to-bin solar spectral uncertainty over the Al/Nb/C channel pass band is approximately 30% in the 0.1–7-nm range and 5% in the 17–22-nm range. The FISM-M spectra and uncertainties are described in detail in Thiemann, Chamberlin, et al. (2017). EUV spectral irradiance can vary rapidly and significantly during solar flares (e.g., Thiemann, Chamberlin, et al., 2017; Thiemann, Eparvier, et al., 2017; Woods et al., 2011); therefore, occultations occurring during flares are neglected. Note that the absolute uncertainty in spectral irradiance does not matter for solar occultations since the measurements are normalized by their value at the top of the atmosphere.

The CO<sub>2</sub> cross sections used are from Huestis and Berkowitz (2011), correspond with a temperature of 300 K, and increase smoothly by a factor of ~2.5 from 17 to 22 nm.

The radiance over the solar disk in the Al/Nb/C channel band pass is approximated as being the same as that in the band pass of the 17.4-nm SWAP (Sun Watcher using Active Pixel system and image processing) telescope (Bougher et al., 2006; Seaton et al., 2013) onboard the Project for OnBoard Autonomy 2 (PROBA2) Earth orbiting satellite. This approximation is valid because emissions measured in both instruments' band passes are dominated by plasmas forming at similar temperatures (Bougher et al., 2006; Thiemann, Chamberlin, et al., 2017). Earth measured images are interpolated to Mars for a given day by time-shifting earlier and later images from Earth using the irradiance interpolation method described in Thiemann, Chamberlin, et al. (2017), which interpolates irradiance assuming it varies on solar rotation timescales. Images used are measured nearest to 12:00 UT that are also at least 2 hr after a C-class or larger solar flare.

The image interpolation method has some error associated with it because the radiance on the solar disk also evolves due to processes occurring on timescales shorter than that of the solar rotation (e.g., active region emergence and decay). This error is estimated by comparing SWAP images measured on a given day, say,  $t_d$ , with predicted images found by averaging SWAP images from one solar rotation prior (day  $t_d - 27$ ) and one solar rotation later (day  $t_d + 27$ ). Since equation (1) inherently assumes that the Mars thermosphere is horizontally stratified, the solar disk is inherently integrated in the direction parallel to the Martian surface. Figure 3 shows this uncertainty as a function of the subtended angle from disk center, along an axis in the

zenith direction that bisects the solar disk. Note that the solar corona extends beyond the visible disk, which subtends an angle of  $0.52^\circ$  at 1 AU.

#### 4. Density Retrieval Uncertainty

The EUVM-SO density uncertainty and systematic error are estimated with Monte Carlo (MC) analysis. Ad hoc “ground-truth” atmospheres are synthesized over the range of densities observed in the EUVM-SO data set and compositions (only  $\text{CO}_2$  and O are considered) expected to occur in the Mars thermosphere. The  $\text{CO}_2$  density profiles are synthesized by adding two decaying exponential functions of the form  $n(\mathbf{z}) \cong n(\mathbf{z}_0) \exp\left(-(\mathbf{z}-\mathbf{z}_0) \frac{m_{\text{CO}_2} g}{kT}\right)$  with  $z_0$  equal to 100 and 150 km.  $n(z_0)$  for the lower (upper) exponential term is  $5 \times 10^{12}$  ( $5 \times 10^9$ )  $\text{cm}^{-3} \pm 50\%$  ( $1 - \sigma$ ) with a lower limit of  $10^{10}$  ( $10^7$ )  $\text{cm}^{-3}$ .  $T$  for the lower exponential term is  $100 \text{ K} \pm 80\%$  with a lower limit of 7 K, and  $T$  for the upper exponential term is 2.5x that of the lower exponential term with an additional 50% randomization and a lower limit of 150 K. The O density profiles are synthesized with a single exponential function of the same form as that used for  $\text{CO}_2$ , with O density fixed to be 1% of the  $\text{CO}_2$  density at 150 km and the same temperature as the upper exponential  $\text{CO}_2$  density term. Figures 4b and 4c show the mean  $\text{CO}_2$  density and O/ $\text{CO}_2$  density ratio with solid curves and the corresponding  $\pm 1 - \sigma$  range with dashed curves.

The ground-truth densities are then input to a measurement model of the Al/Nb/C channel to synthesize extinction ratios. Note that the O photoabsorption cross sections are from the PHotolization/Dissociation Rates (PHIDRATES) database (Huebner & Mukherjee, 2015). Densities are then retrieved from these extinction ratios and compared to the ground-truth densities to quantify the random uncertainty and systematic error in the measurement.

The uncertainty analysis includes the following sources of random uncertainty or systematic error: measurement noise, uncertainty in the instrument response function, nonflaring solar variability, solar spectral uncertainty,  $\text{CO}_2$  cross section uncertainty, image interpolation uncertainty, and uncertainty in the retrieval algorithms. The measurement noise is very small and approximately 30 ppm of the measured signal (Thiemann, 2016). The  $\text{CO}_2$  cross section uncertainty at the measurement wavelengths is 5% (Gallagher et al., 1988). The typical nonflaring solar variability estimate is taken from Thiemann, Dominique, et al. (2017), who quantified the typical nonflaring EUV variability below 20 nm over solar occultation timescales and found it to be 0.35% over a 2-min occultation scan. All other uncertainties are discussed in section 3, except for that of the retrieval algorithm itself, which is inherently characterized by the MC analysis.

Uncertainty in the cross section and response function results in systematic errors in the density retrieval that depends on the sign of the respective uncertainty (i.e., whether the response function or cross sections are actually smaller or larger than estimated). Because of this, the systematic error is simulated for two cases, spanning the possible range of the summed systematic errors. The total systematic error is bounded by both cases.

Figure 4a shows the results of the MC uncertainty analysis over the density range that the EUVM-SO measurements are sensitive. On the right-hand side of the figure, approximate corresponding altitudes at perihelion and aphelion are shown. The solid curve corresponds with the random uncertainty and is due to signal strength, instrument noise, solar variability, and uncertainty in the solar spectrum. The random uncertainty is between 5% and 10% over much of the density range but becomes larger at the highest and lowest densities. This is where the extinction ratio is close to 0 or 1, respectively, and the change in the extinction ratio with altitude near these extremes becomes comparable to the magnitude of random variations in the signal. The dashed curves are the envelope that bounds the systematic error. As discussed above, the systematic error is ill-defined because of the uncertainty in the response function. At intermediate densities and altitudes, the systematic error is somewhere between approximately 5% and 22%. At low densities and high altitudes, the systematic error becomes large due to extinction from unaccounted O, which becomes increasingly substantial with increasing altitude. At high densities and low altitudes, the systematic error becomes large due to the assumption of a single-scale height atmosphere, when a second scale height corresponding with the cold mesopause dominates at lower altitudes. In principle, the systematic error could be applied to the data as a correction, especially at intermediate altitudes, where the mean value varies gradually from  $-10\%$  to  $-20\%$ . This is not done in the data presented here as it

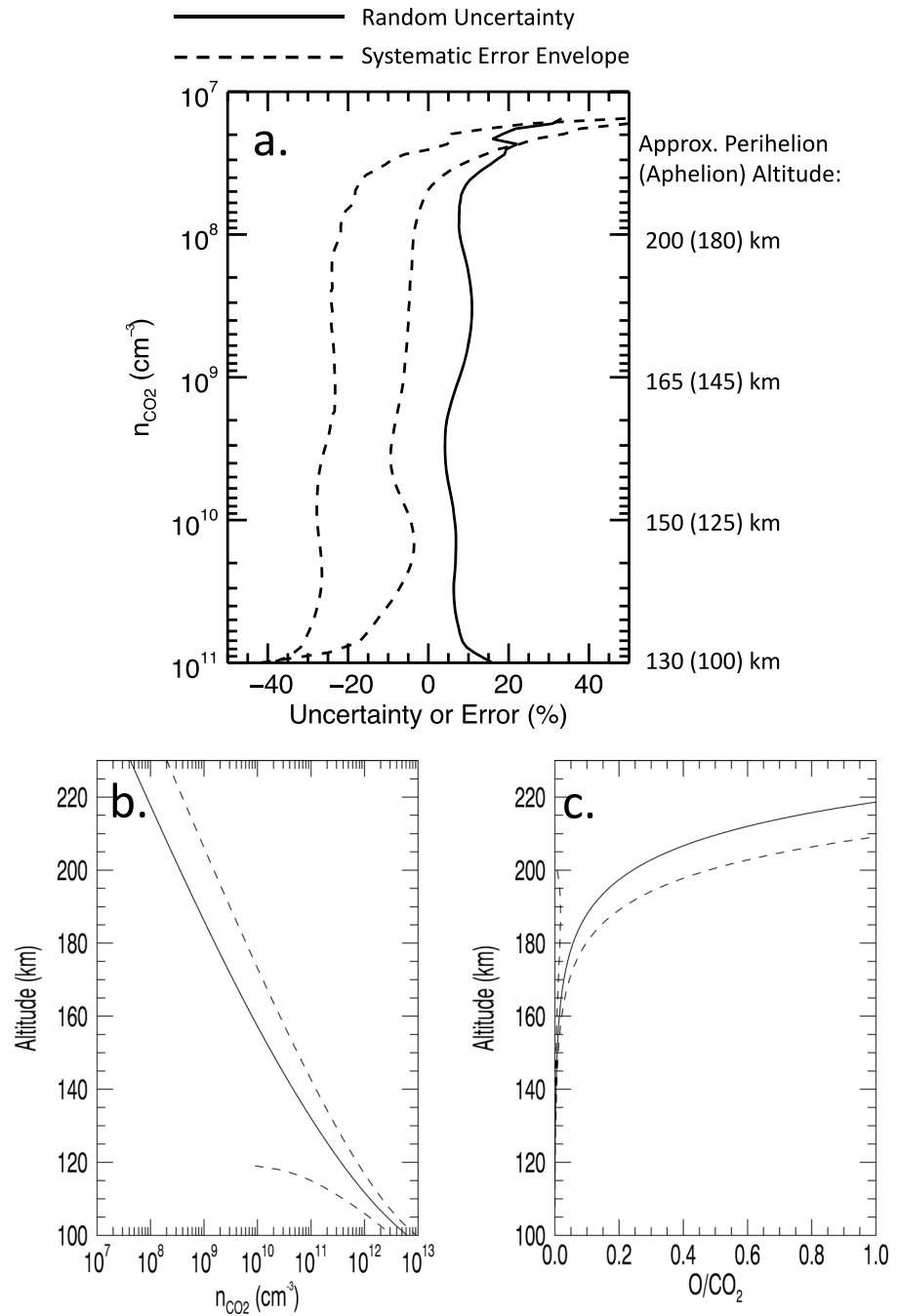


**Figure 4.** (a) Extreme Ultraviolet Monitor solar occultation random uncertainty (solid curve) and systematic error (dashed curves) versus CO<sub>2</sub> number density. The systematic error is bounded by the two dashed curves shown and is ill-defined because the sign of any systematic error in the response function is unknown. On the right-hand side, approximate altitudes corresponding with density at perihelion (aphelion) are shown. The average and standard deviation for the ground-truth density profiles (b) and O/CO<sub>2</sub> density ratios (c) are shown with solid and dashed curves, respectively.

does not impact the conclusions but may be done in future public releases of these data, so data users should take care to inspect the systematic error profiles associated with the data.

The random uncertainty and systematic error have implications for how the EUVM-SO profiles are interpreted. Clearly, data at the altitude and density extremes need to be treated with caution. For intermediate altitudes, the systematic error could be removed from the data to improve accuracy using

the profile(s) shown in Figure 4. This is not done for the data presented in section 5 because doing so would not materially change the conclusions. Instead, the estimated systematic error is conservatively treated as an additional uncertainty. The small random uncertainty across the majority of the sensitivity range indicates that the EUVM-SO data are ideal for tracking relative changes. In particular, the small random uncertainty in the density profiles indicate that relatively small temperature changes are resolvable given the logarithmic dependence of temperature on density for an atmosphere in hydrostatic equilibrium.

Thiemann, Dominique, et al. (2017) performed a nearly identical MC uncertainty analysis for the LYRA solar occultation measurements at Earth. The two differences in their analysis are that they omitted the response function uncertainty because it was known to remain within 1% due to a more precise prelaunch calibration, and they had an additional systematic uncertainty associated with assuming equivalent cross sections for  $N_2$  and O. Nevertheless, the uncertainties for LYRA are comparable to those shown for EUVM in Figure 4. Further, Thiemann, Dominique, et al. (2017) found better than 5% agreement with the LYRA measurements and predictions made by the NRLMSISE-00 empirical model for Earth's thermospheric density (Picone et al., 2002), which has been independently characterized and validated by available thermospheric density measurements at the Earth. The good agreement between LYRA solar occultation observations and NRLMSISE-00 predictions also serve to validate the EUVM-SO observations given the similarities in the instruments and near identical retrieval algorithms.

Additionally, if the observing latitude varies substantially during an occultation scan, as occurs when the spacecraft  $\beta$  angle approaches  $90^\circ$ , the retrieved densities no longer correspond with a vertical profile. This has no significant effect on the density retrieval (Thiemann, Dominique, et al., 2017), but because the temperature calculation assumes a vertical density profile, substantial error can be introduced to derived temperatures when the scan spans a large range of latitudes. We adopt the upper limit of a  $4^\circ$  change in latitude during an occultation scan for valid temperature calculations based on the fact that in the winter hemisphere, where latitudinal temperature gradients are steeper, temperature varies by less than 10 K over  $4^\circ$  latitude (e.g., González-Galindo, Forget, López-Valverde, Angelats i Coll, & Millour, 2009) or  $\sim 10\%$  of the expected vertical temperature variation over the EUVM-SO measurement range.

## 5. Results

At the time of this writing, over 2,000 density profiles have been retrieved from EUVM-SO measurements, providing a unique data set for studying the structure and variability of the Mars thermosphere. It would be unwieldy to present the data set in its entirety in a single paper. As such, the focus of this section is to present a subset of the observations that provide new insight into the structure of the Mars thermosphere and its variability, while highlighting the utility and novelty of the data set. Specifically, this section presents measurements of (i) the temperature and density structure of the northern hemisphere near aphelion at both dawn and dusk terminators; (ii) the temperature and density structure in the dusk terminator near perihelion; and (iii) the correlation between thermospheric temperature variability and solar variability.

In general, solar EUV heating, planetary rotation, and tidal, planetary, and gravity wave forcing from below determine the density and temperature structure of the thermosphere, resulting in regional temperature and density enhancements or depletions (Bougher, 1995; Bougher et al., 2002; Bougher, Cravens, et al., 2015). The thermospheric structure has been studied using a number of Mars specific general circulation models (GCMs), including the Mars Thermosphere GCM (Bougher et al., 1999, 2000), the Laboratoire de Météorologie Dynamique Mars GCM (González-Galindo, Forget, López-Valverde, Angelats i Coll, & Millour, 2009; González-Galindo, Forget, López-Valverde, & Angelats i Coll, 2009), and the Mars Global Ionosphere Thermosphere Model (Bougher, Pawlowski, et al., 2015). Throughout the following data presentation, GCM results are referenced to aid the interpretation of features observed in the EUVM-SO data. These comparisons are predominantly qualitative and hindered by the lack of previously published scenarios that exactly correspond with that observed by the EUVM-SOs. A more complete understanding of the features in the EUVM-SO data can be gained by direct GCM to measurement comparisons and will be the topic of future studies.

Figure 5 provides an overview of the EUVM measurements made and processed at the time of this writing. Figure 5a shows inferred thermospheric temperature at 585 nPa ( $T_{595}$ ; approximately 150 km at perihelion) versus time at the dawn and dusk terminators with blue and red asterisks, respectively; also shown in this figure is the inverse Mars-Sun distance squared ( $1/R^2$ ) with green asterisks, which is proportional to solar

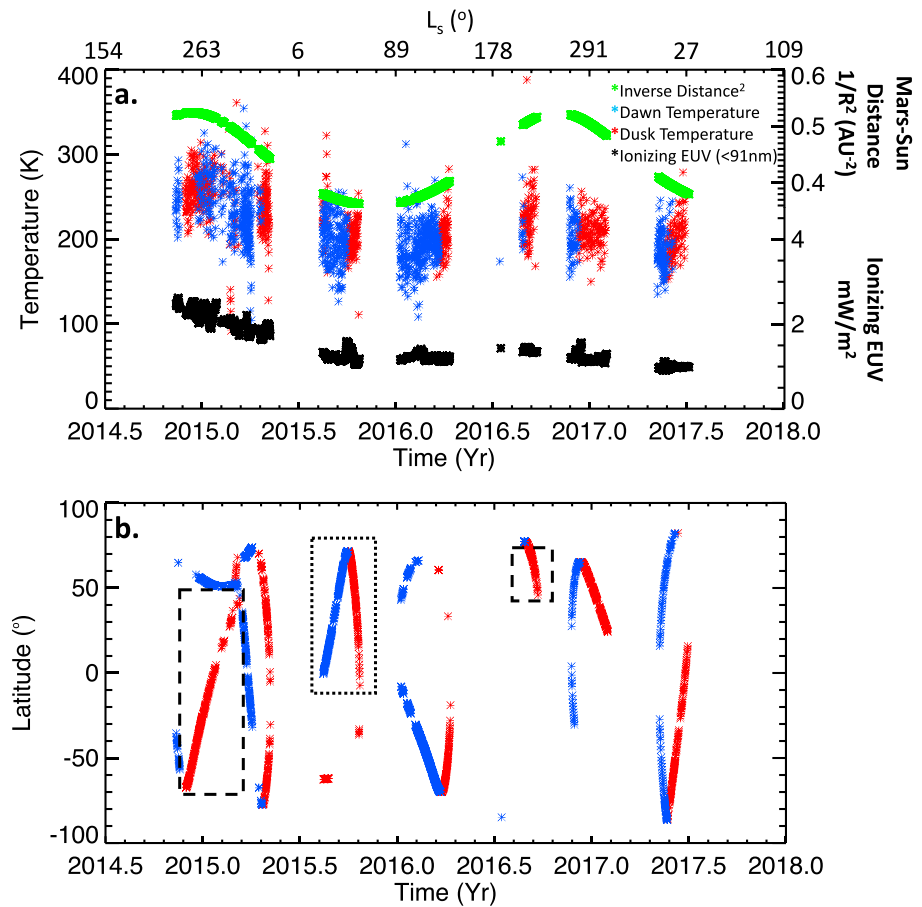


**Figure 5.** Thermospheric temperature variability observed by MAVEN Extreme Ultraviolet (EUV) Monitor (EUVM) solar occultation measurements. (a) Dawn and dusk temperatures at 595 nPa are shown with blue and red asterisks, respectively. Also shown are measures of solar variability, with the green asterisks showing the inverse Mars-Sun distance squared,  $1/R^2$ , and the black asterisks showing  $\text{CO}_2$  ionizing EUV radiation,  $E_{\text{EUV}}$ . (b) Latitudes of where the EUVM observations are made, where blue and red asterisks again correspond with measurements at the dawn and dusk terminators, respectively. The data in the dotted box are analyzed in section 5.2, and the data in the dashed boxes are analyzed in section 5.1.

insolation, and the corresponding 0–93-nm  $\text{CO}_2$ -ionizing EUV irradiance ( $E_{\text{EUV}}$ ) with black asterisks, which is derived from the EUVM Level 3 data product (Thiemann, Chamberlin, et al., 2017). Comparing the  $T_{595}$  measurements with the solar values reveals a clear correlation between them, which will be investigated further in section 5.3. Figure 5b shows the latitudes corresponding with the temperature measurements using the same color as in Figure 5a. The MAVEN orbit precession results in EUVM-SO measurements being made over a range of latitudes within a relatively short time. As a result, EUVM is capable of scanning a wide range of latitudes during which the seasonal changes are relatively small, enabling the profiling of the entire hemispheres at fixed local time and approximately fixed season. This capability is exploited next in sections 5.1 and 5.2, where maps of thermospheric structure near aphelion and perihelion are presented.

### 5.1. Mars Thermospheric Structure Near Aphelion: Northern Dawn and Dusk Terminators

Between early August and early November of 2015, EUVM-SOs scanned much of the northern hemisphere, beginning near the dawn equator, moving over the north pole, and finishing near the dusk equator. During this time, the Mars solar longitude,  $L_s$ , varied from  $23.2^\circ$  to  $64.5^\circ$ , corresponding with mid-spring in the northern hemisphere, as the planet approached aphelion (occurring at  $L_s = 71^\circ$ ). The nonzero solar declination during this time resulted in EUVM-SOs observing a maximum latitude of  $71.6^\circ\text{N}$  as the observations passed behind the pole at the dawn-dusk transition.

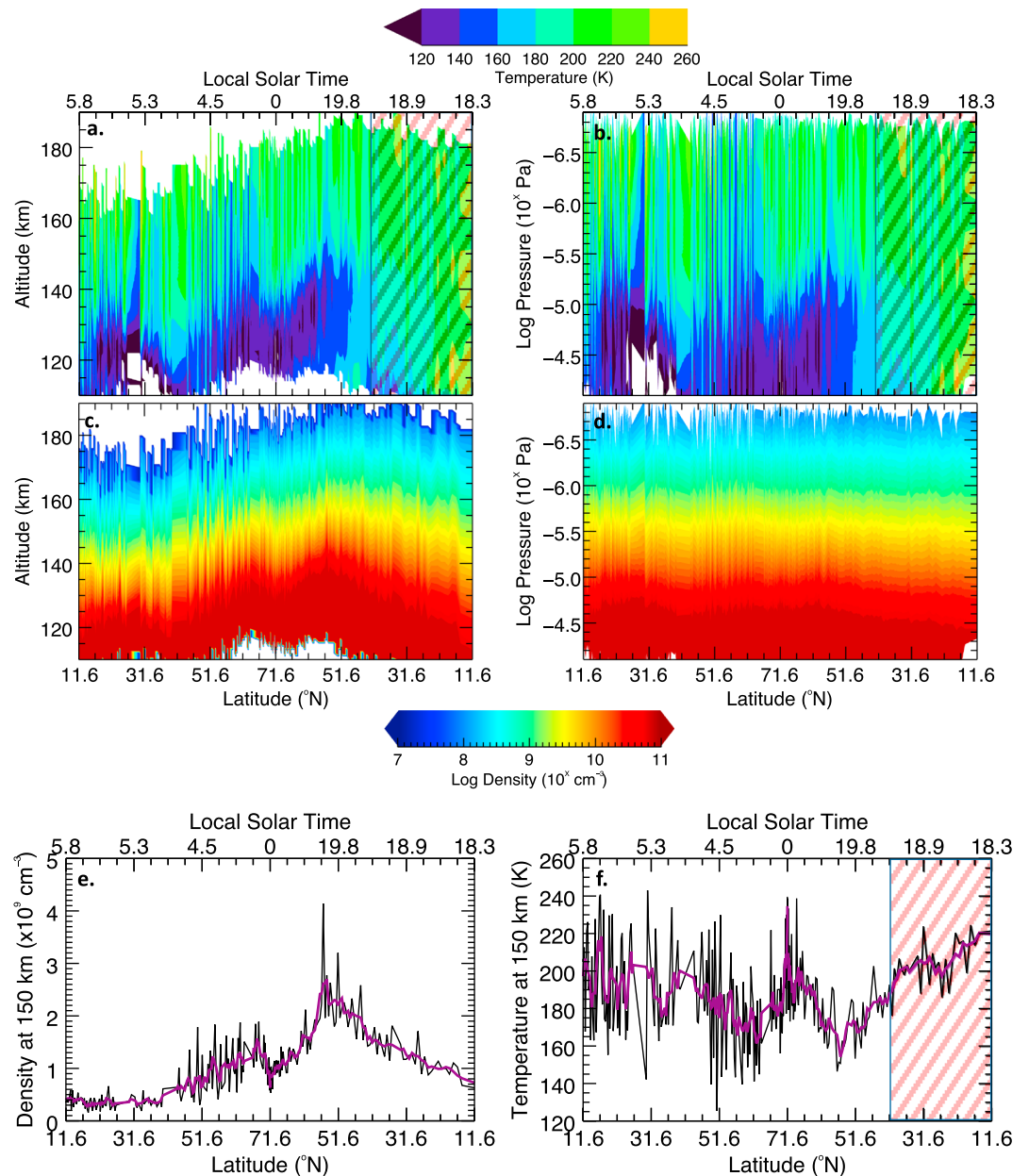


**Figure 6.** Thermospheric temperature and density near aphelion measured by Extreme Ultraviolet Monitor solar occultations. Panels a (c) and b (d) show temperature (density) as a function of latitude and altitude or pressure, respectively. The bottom horizontal axis shows latitude. Ambiguity in latitude between the dawn and dusk terminators can be resolved with the top horizontal axis, which gives the local solar time. Panels (e) and (f) show density and temperature at 150 km, with black curves corresponding with individual orbits and purple with the 5-orbit running average.

Figure 6 shows EUVM-SO measured temperatures and densities from this time period, where Figures 6a (c) and 6b (d) show temperature (density) as a function of latitude versus altitude or pressure, respectively. The bottom horizontal axis shows the corresponding latitude. Ambiguity in dusk versus dawn latitudes is resolved with the top horizontal axis, which gives the corresponding local solar time. Figures 6e and 6f show density and temperature, respectively, at 150 km, where black curves correspond with individual orbits and purple with the 5-orbit running mean. Note that the mean latitude is used for each occultation scan, resulting in the density or temperature from each occultation scan being (artificially) rendered as perfectly vertical in Figure 6. The overlaid hatch pattern in Figures 6a and 6b corresponds with scans where the latitude varies by 4° or more, implying the derived temperatures are prone to error as discussed in section 4.

The temperature and density maps shown in Figure 6 reveal similarities and differences between the dawn and dusk terminators. The temperature magnitude and variation with altitude shown in Figure 6a are in general agreement with GCM predictions at 04:00 and 15:00 LST by Bougher et al. (1999). Examining the highest altitudes where measurements are available in Figure 6c reveals a substantial 20–30-km dusk bulge, which can be attributed to diurnal variability to first order because, prior to observation, the dusk atmosphere is rotating from the solar EUV heated dayside, while the dawn atmosphere is rotating from the cold nightside (Bougher et al., 1999). Additionally, the dawn terminator is more variable than the dusk terminator as can be seen in Figures 6a and 6b by a marked increase of high frequency structure at high altitudes at the dawn terminator; this is consistent with recent observations reported in Zurek et al. (2017) showing larger mass density variability at dawn than dusk below 150 km. This high frequency variability may be more temporal than latitudinal in nature given that these maps are constructed over many orbits. Simulations of the Mars thermospheric structure near the equinoxes indicate a much steeper temperature gradient at dawn relative to dusk (Bougher et al., 1999; Bougher, Pawlowski, et al., 2015; González-Galindo, Forget, López-Valverde, Angelats i Coll, & Millour, 2009), which may partially explain the increased temperature variability observed at dawn.

Specifically, this temporal variability may be due to gravity waves, which are expected to have a greater influence on thermospheric temperature when vertical temperature gradients and, hence, kinematic viscosity gradients increase (Vadas et al., 2014). Enhanced gravity wave activity near the dawn terminator is supported by simulations (Yigit, England, et al., 2015) and recent observations (Terada et al., 2017). Figure 6d shows increased orbit-to-orbit density variability clustered around  $\sim 55^\circ\text{N}$  at both terminators. These same latitudes correspond with a 20–30 K drop in temperature relative to that at  $71.6^\circ\text{N}$  and may be evidence of high-latitude gravity wave induced cooling predicted by some simulations (Medvedev et al., 2015; Medvedev & Yigit, 2012; Yigit, Medvedev et al., 2015).

At a fixed altitude, density increases due to either bulk atmospheric expansion or local heating. At constant pressure, the ideal gas law requires decreasing density to correspond with increasing temperature and presumably increasing heating. As such, plotting density versus pressure controls for changes due to bulk atmospheric expansion (or contraction), isolating local heating (or cooling). Figure 6d shows a decrease in density at  $10^{-5}$  Pa moving equatorward on the dusk terminator, indicating local heating is increasing away from the north pole. A temperature maximum is expected due to solar heating at subsolar latitudes, both directly by increasing EUV heating of the thermosphere and indirectly by decreasing molecular conduction as a result of increased IR heating at lower altitudes (Bougher et al., 1999, 2000). Figure 6d also shows a decrease in density near  $40^\circ\text{N}$  on the dawnside, and Figures 6a and 6b show a corresponding temperature increase, indicating that local heating is occurring here. This feature may be evidence of adiabatic heating from solar driven zonal circulation that is expected to drive upwelling (and adiabatic cooling) in the afternoon sector resulting in subsidence (and adiabatic heating) in the post-midnight sector near subsolar latitudes, resulting in a “tongue” of increased temperature extending toward dawn (Bougher et al., 1999).

## 5.2. Mars Dusk Thermospheric Structure Near Perihelion

MAVEN was at Mars during the perihelions of MY 32 and 33, occurring near the end of 2014 and 2016, respectively. EUVM scanned the dusk terminator from  $67^\circ\text{S}$  to  $30^\circ\text{N}$  between early December 2014 and mid-February 2015, during which the Mars  $L_s$  precessed from  $244^\circ$  to  $291^\circ$ , encompassing both perihelion (at  $L_s = 251^\circ$ ) and the Northern Winter Solstice (at  $L_s = 270^\circ$ ). During MY 33, EUVM scanned from  $70^\circ\text{N}$  to  $30^\circ\text{N}$  between mid-September 2016 and mid-January 2017, during which the Mars  $L_s$  precessed from  $223^\circ$  to  $299^\circ$ . Data from both of these periods are used to construct the maps of temperature and density at the dusk terminator shown in Figure 7, where the panel arrangement is the same as Figure 6, but the LST axis is omitted because all data are at dusk. Data southward of  $30^\circ\text{N}$  were measured during MY 32, and the remaining data were measured during MY 33. The two data gaps between  $5^\circ\text{N}$  and  $30^\circ\text{N}$  coincide with when EUVM was not sun pointed.

Figure 7c shows a large-scale trend of decreasing density at high altitudes from the southernmost latitudes to the northernmost latitudes. This trend disappears in Figure 7d, indicating the southern, summer hemisphere is inflated relative to the northern, winter hemisphere. The high-altitude (exospheric) temperatures are near 250 K from the southernmost latitudes to the low-latitude northern hemisphere. Above  $30^\circ\text{N}$ , exospheric temperatures are near 200 K, except for between  $52^\circ\text{N}$  and  $62^\circ\text{N}$  where the exospheric temperature increases to 260 K. This temperature enhancement is most pronounced above 170 km but extends to the lower

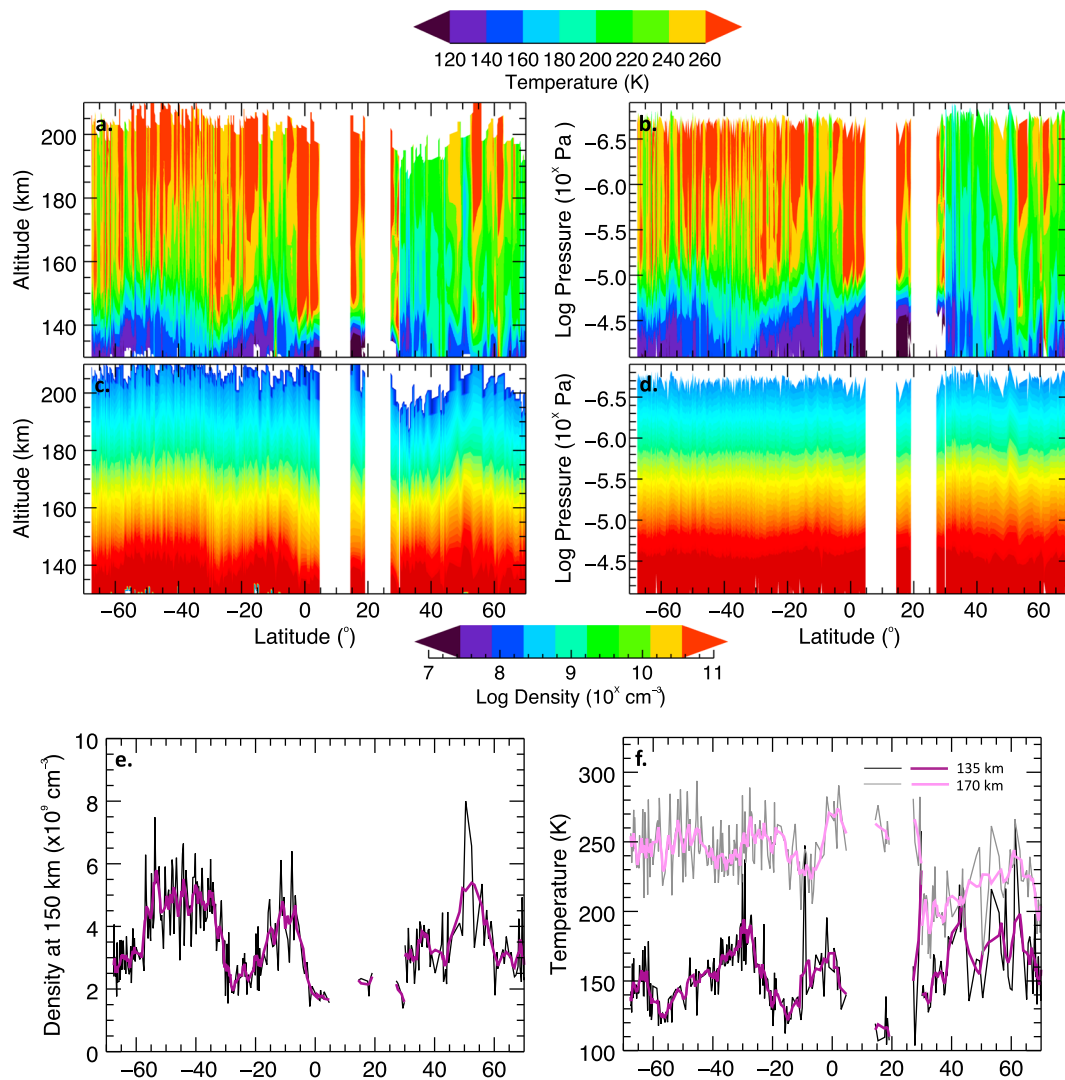


**Figure 7.** Thermospheric temperature and density at the dusk terminator near perihelion measured by EUVM-SOs. Same panel arrangement as Figure 6.

thermosphere. This feature is consistent with “polar warming” features predicted to occur at intermediate latitudes during northern winter that result from enhanced interhemispheric circulation during perihelion (e.g., Bell et al., 2007; González-Galindo et al., 2015). This circulation is enhanced during the dust season and results in localized adiabatic heating at the North Pole and near 50°N, where the latter is concentrated at higher altitudes. For examples of simulations of this feature and underlying heating rates, see Figures 6 and 7 in Bell et al. (2007) and Figure 11 in González-Galindo, Forget, López-Valverde, and Angelats i Coll (2009). Previously, limited “polar warming” features ( $\Delta T \sim 40\text{--}60$  K) were observed during Odyssey aerobraking ( $L_s \sim 260\text{--}310$ ) only at 120 km at high northern latitudes ( $\sim 60\text{--}80$  N; Bougher et al., 2006; Bougher, Brain, et al., 2017).

Although not obvious at the resolution shown in Figure 7, a close inspection of the data (not shown here) reveals periodic temperature and density fluctuations with periods of approximately 2 days or, equivalently,  $2^\circ$  in latitude. These may be due to nonmigrating tides resulting in enhancements at fixed geographic latitudes that rotate past the terminator while EUVM is making observations. Further analysis is needed to understand the nature of these oscillations and correct for any aliasing caused by the observing cadence.

Figure 7c shows two density maxima between 0 and 60°S at 140 km that correspond with pronounced temperature decreases at the same altitude seen in Figure 7a. Although these structures may be latitudinal in nature, there is no obvious correspondence with features arising in published GCM results of the Mars

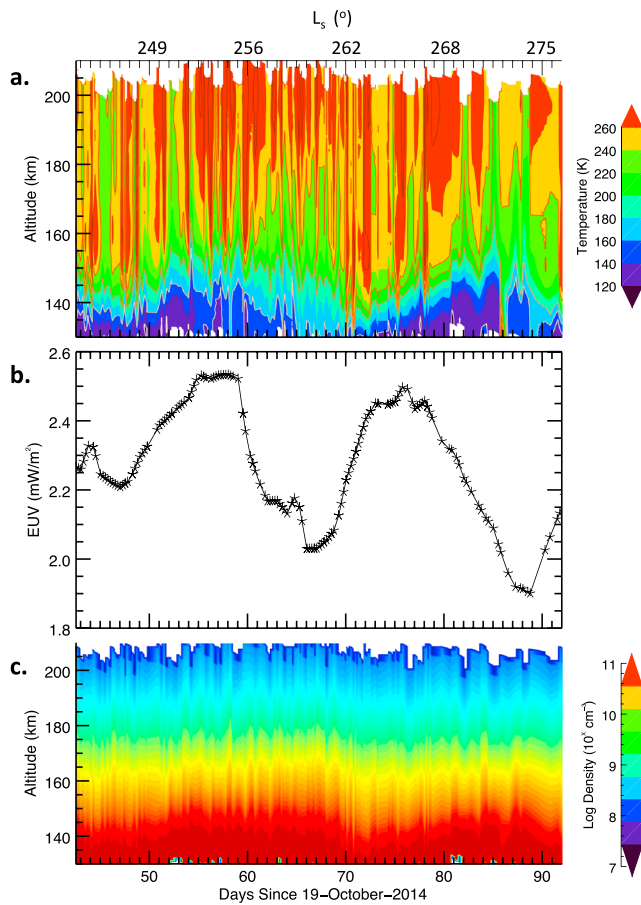


**Figure 8.** Correlation between density and temperature structure and extreme ultraviolet (EUV) irradiance. (a) Thermospheric temperature versus altitude and time. Temperature is correlated with EUV irradiance above the black-dashed contour but anticorrelated with EUV irradiance below the white dashed contour. (b) Corresponding 0–93 nm integrated EUV irradiance. (c) Corresponding thermospheric density.

thermosphere near perihelion (Bougher et al., 2000; Bougher, Pawlowski, et al., 2015; González-Galindo, Forget, López-Valverde, & Angelats i Coll, 2009). Rather, they are believed to be temporal in nature and the result of solar variability because they are co-incident in time with a strong modulation of EUV irradiance due to solar rotation.

Figures 8a and 8c replot the southern hemisphere temperature and density data from Figures 7a and 7c, respectively, as functions of time rather than latitude, with the horizontal axis corresponding with days since 19 October 2014. Figure 8b shows the corresponding  $E_{\text{EUV}}$  from the EUVM Level 3 data product, which shows that  $E_{\text{EUV}}$  varied by 20% with a ~27-day period over this time. Two contours are drawn on Figure 8a to guide the eye to regions of heating and cooling in the thermosphere. Above the black dashed contour, there is a ~27-day heating trend, where temperature increases with increasing EUV irradiance. At lower altitudes, below the dashed white contour, the opposite trend occurs, where temperature decreases with increasing EUV irradiance prior to day ~80. The phase differences can be seen clearly in Figure 7f, which shows temperatures at 135 and 170 km, where the thin curves correspond with individual orbit values and the thicker purple and violet curves correspond with the 5-orbit running average. At 170 km, the running average values vary by ~20 K, which is in excellent agreement with predicted and measured variations in exospheric temperature due to solar rotation variability by González-Galindo et al. (2015) and Forbes et al. (2006), who found values near 25 and 19.2 K, respectively. The apparent anticorrelation of temperature at 135 km and EUV variability has not been previously predicted nor observed during solar rotations. However, somewhat similar behavior was predicted by Bougher et al. (1999) using the Mars Thermosphere GCM to simulate the response of the Mars thermosphere to a step-function increase in EUV irradiance, where it was shown that direct heating by EUV irradiance near the altitude of peak EUV heating (~160 km) causes the temperature to increase at high altitudes, causing an expansion of the upper thermosphere. This expansion, in turn, causes the lower thermosphere to cool adiabatically via increasing upward vertical winds, providing a “vertical wind thermostat” that controls the temperature response of the thermosphere due to EUV heating.

Features like those appearing below the white dashed contour in Figure 8a could, in theory, also be caused by regional dust activity that causes an expansion of the lower atmosphere (as a result of increased heating from an elevated opacity), which in turn can lift the mesopause altitude, resulting in a colder, denser atmosphere at a fixed altitude in the lower thermosphere. Dust opacity data for MY 32 is examined to understand the contemporary dust activity. These data are produced using the method of Montabone et al. (2015), which uses measurements made by the Thermal Emission Imaging System (THEMIS) instrument onboard Mars Odyssey and the Mars Climate Sounder (MCS) onboard the Mars Reconnaissance Orbiter (MRO), and are publicly distributed on the web at [http://www-mars.lmd.jussieu.fr/mars/dust\\_climatology/](http://www-mars.lmd.jussieu.fr/mars/dust_climatology/). These data are shown in Figure 9a, which shows the zonal mean 15  $\mu\text{m}$  opacity at 610 Pa versus latitude and  $L_s$ . There is a local maximum opacity of 0.5 near 50°S, which is coincident in latitude with density enhancements and temperature depletions shown in Figure 8. However, this occurred 20 days prior to when EUVM-SOs began for the period shown. By the time EUVM-SO measurements of the southern hemisphere began, the opacity at 50°S decayed to 0.25 and gradually increases to a value of 0.35 at the equator. To evaluate whether this dust activity is expected to result in latent heating capable of causing the structures in lower thermosphere shown in Figure 8, GCM simulations from the Mars Climate Database (Forget et al., 1999; Madeleine et al., 2011; Millour et al., 2015) are evaluated for the corresponding times and latitudes using contemporary (MY 32) dust and solar EUV conditions. Figure 9b shows the Mars Climate Database predictions of temperature between 60 and 200 km, corresponding with the data shown in Figures 7 and 8. The simulations do not predict structures

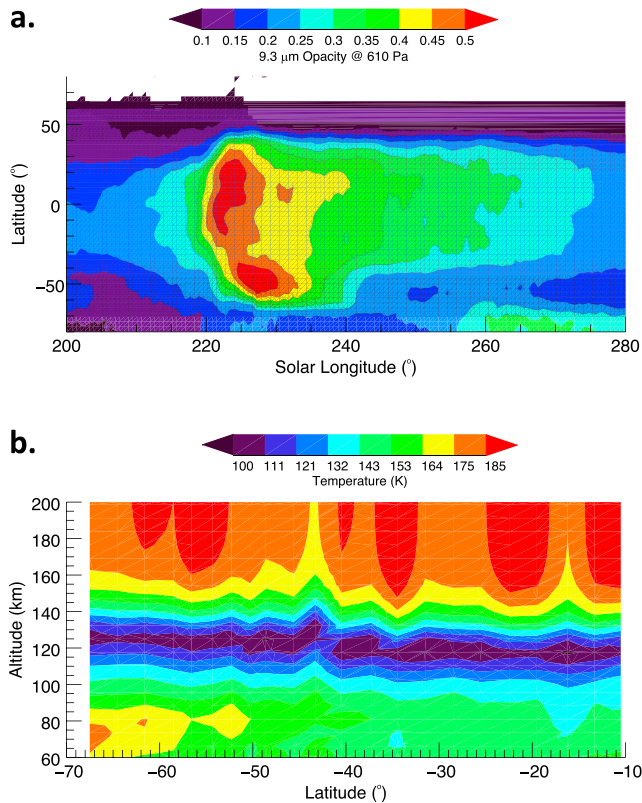


**Figure 9.** Mars year 32 dust activity and predicted atmospheric response for the time and latitudes of Extreme Ultraviolet Monitor solar occultation measurements. (a) Distribution of dust versus latitude and solar longitude as measured by 9.3- $\mu\text{m}$  vertical column opacity normalized to 610 Pa. (b) Mars Climate Database simulations of temperature near the mesopause corresponding with the data shown in Figure 8.

consistent with those observed in Figure 8a, suggesting that they are not a result of latent effects from earlier dust activity at these altitudes and supporting the conclusion that the observed lower thermospheric cooling is a result of EUV solar rotation variability.

### 5.3. The Correlation Between Thermospheric Temperature and Solar Variability

Given that the EUVM-SO measurements span two Mars years, during which solar EUV irradiance decreases from solar moderate to solar minimum levels, they provide an opportunity to characterize the dependence of thermospheric temperature on both solar insolation and EUV forcing, where the former is indicative of seasonal forcing on the thermosphere from below and the latter is indicative of direct heating of the thermosphere. Figure 5a shows the thermospheric temperature at 595 nPa,  $T_{595}$ , along with  $E_{\text{EUV}}$  and  $1/R^2$ . The 595-nPa pressure level coincides with approximately 150 km at periapsis and is selected because it sits in between the altitude of expected peak EUV heating near 170 km and peak EUV energy deposition near 130 km (Bougher et al., 1999; González-Galindo et al., 2005). Although  $E_{\text{EUV}}$  variability reflects the  $1/R^2$  variability, the long-term decreasing solar variability dominates, resulting in a 50% reduction of  $E_{\text{EUV}}$  for the second perihelion as compared to the first perihelion shown. As such, these data should contain adequate variability to decouple the dependence of  $T_{595}$  on  $E_{\text{EUV}}$  and  $1/R^2$ .

For each terminator, temperatures in four narrow latitude bands are compared with  $E_{\text{EUV}}$  and  $1/R^2$ , where the latitude bands are chosen to maximize repeat measurements across the available time range. Figure 10 shows  $T_{595}$  and solar variability comparisons for the dusk terminator. The left column shows scatterplots of  $T_{595}$  versus  $E_{\text{EUV}}$ , where the least squares best fit is shown in black and the right column shows scatterplots of  $T_{595}$  versus  $1/R^2$ . The color code indicates the time when the measurements were made. Figure 11 is similar to Figure 10 but for the dawn terminator. For each panel in Figures 10 and 11, the Pearson correlation coefficient,  $r$ , is found and reported in Table 1 along with the thermospheric temperature sensitivity to EUV forcing,  $dT/dE_{\text{EUV}}$ . For each geometry, the larger  $r$  value is underlined in Table 1 if the difference is statistically significant.

Of the eight geometries considered,  $r_{\text{EUV}}$  is larger (smaller) than  $r_{1/R^2}$  for four (two) cases, confirming what is also evident by inspection of Figures 10 and 11: Thermospheric temperature is better correlated with EUV irradiance than solar insolation. This differs from the conclusion of Bougher, Roeten, et al. (2017) who used the MAVEN NGIMS and IUVS instruments to find no significant difference between correlations of thermospheric temperature with  $1/R^2$  or  $E_{\text{EUV}}$ . The difference in conclusions is likely due to Bougher, Roeten, et al. (2017) having used only data between October 2014 and June 2016, a period when the differences between  $E_{\text{EUV}}$  and  $1/R^2$  are relatively small; and the conclusion found here is more complete given the larger extent of data analyzed.

There are some exceptions to better the correlation between  $T_{595}$  and  $E_{\text{EUV}}$  found here, most notably, the 50–60°N dusk case shown in Figure 10. Here the orange-yellow subset of temperatures is warmer than the trend line would suggest. These data correspond with when Mars was at perihelion, which is when polar warming was observed at these same latitudes as discussed in section 5.2. It follows that although EUV irradiance is the primary energy input to the thermosphere, global circulation plays an important role in determining thermospheric temperature. It is also notable that while one might expect a higher correlation between  $E_{\text{EUV}}$  and  $T_{595}$  at dusk because the atmosphere there has been heated by the Sun the preceding half-day, the correlation between  $E_{\text{EUV}}$  and  $T_{595}$  is about the same at either terminator, with the average dusk value of  $r_{\text{EUV}}$  being equal to 0.56 and that at dawn being equal to 0.51.

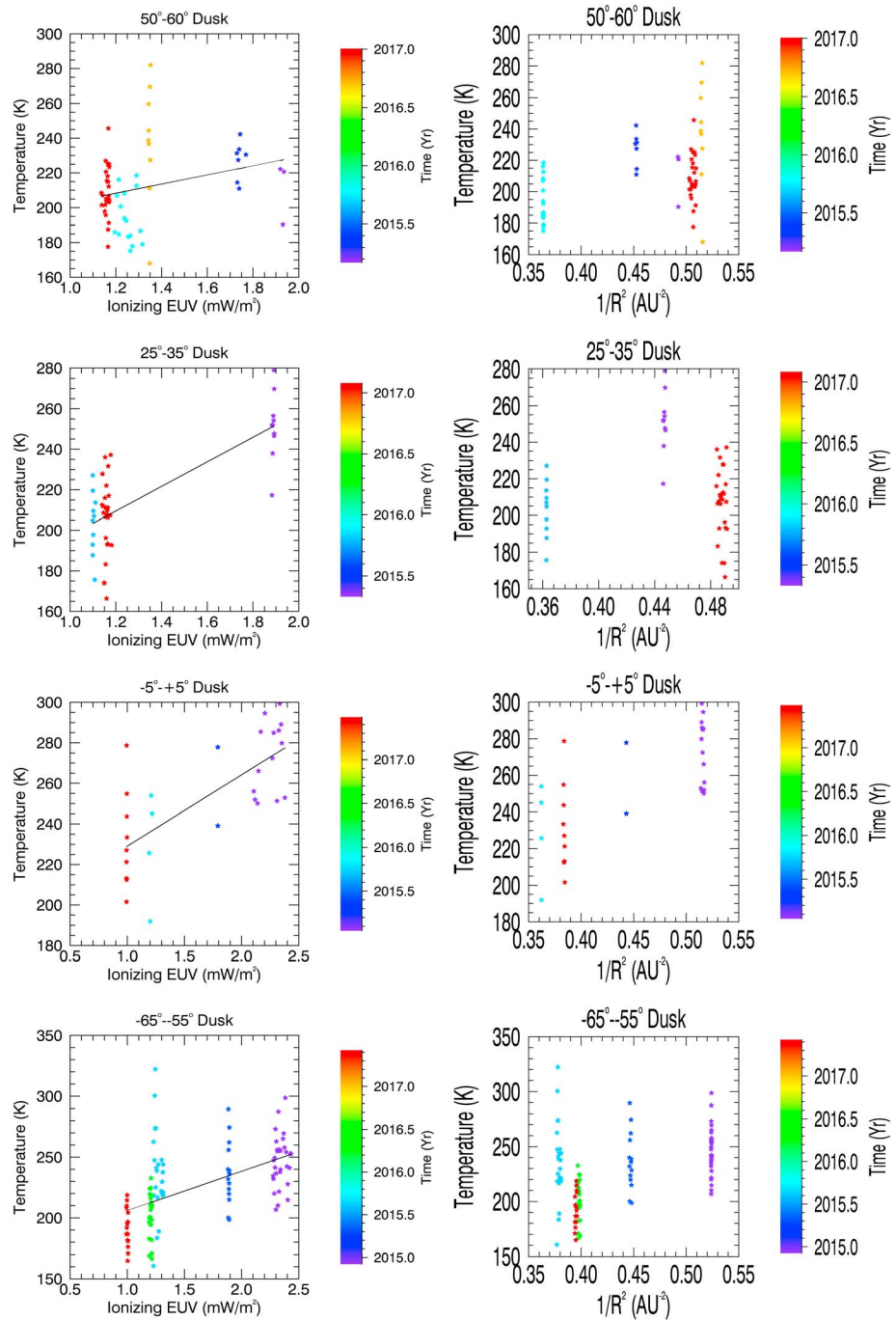


**Figure 10.** Comparisons of thermospheric and solar variability at the dusk terminator. The left column shows scatterplots of  $T_{595}$  versus  $E_{EUV}$ , and the right column shows scatterplots of  $T_{595}$  versus  $1/R^2$ . Each row corresponds with a different latitude range. EUV = extreme ultraviolet.

The average value of  $dT/dE_{EUV}$  is found to be  $45 \pm 12 \text{ K m}^2 \text{ mW}^{-1}$  if the two cases where  $r_{EUV} < 0.3$  are omitted.  $E_{EUV}$  varies from approximately 3.5 to 0.75  $\text{mW/m}^2$  from perihelion at solar maximum to aphelion at solar minimum for a typical solar cycle. A  $dT/dE_{EUV}$  value of  $45 \text{ K m}^2 \text{ mW}^{-1}$  would then correspond with a thermospheric temperature change of 123 K. This value is consistent with the temperature variations predicted by the Mars Global Ionosphere Thermosphere Model at the terminator (Bougher, Pawlowski, et al., 2015), but it should be noted that the variability near the subsolar point is predicted to be about 75 K larger

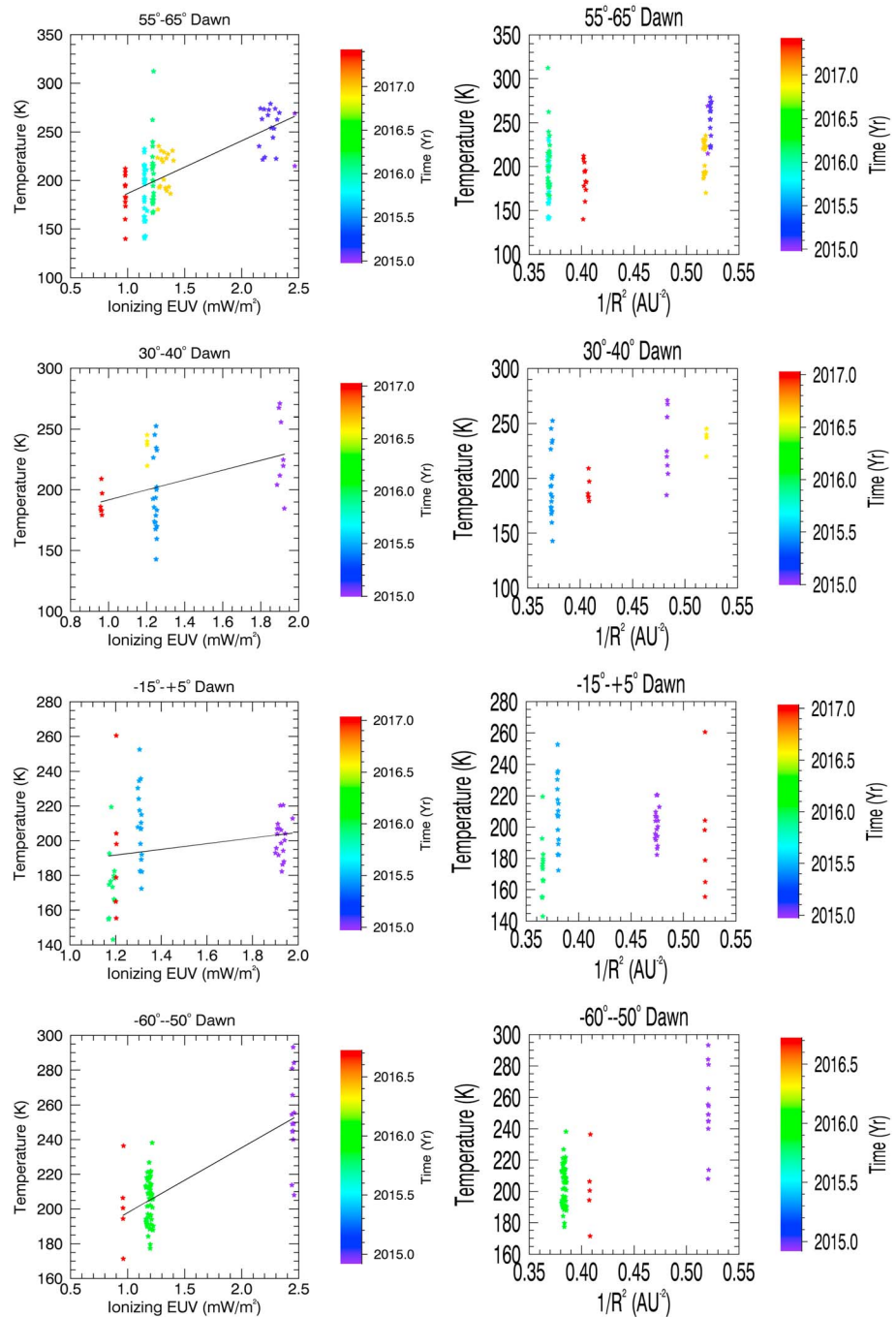


**Figure 11.** Same as Figure 10 but for the dawn terminator.

over the solar cycle, reflecting greater solar EUV control of thermospheric temperature here. González-Galindo et al. (2015) show a more moderate net variation of  $\sim 150$  K at the subsolar point over similar conditions but do not report temperatures near the terminator. Recently, Bougher, Roeten, et al. (2017) used the MAVEN NGIMS and IUVS instruments to find  $dT/dE_{EUV}$  using data from the first MY that MAVEN was at Mars, and it found it to be  $2.25 \text{ km m}^2 \text{ mW}^{-1}$ , where the units are in scaleheight per solar Lyman-alpha irradiance. Converting this value to the units used here yields  $66.7 \text{ K m}^2 \text{ mW}^{-1}$ . This value is somewhat larger than the value found here, and the differences may be a result of Bougher, Roeten, et al. (2017) using data with solar zenith angles less than  $75^\circ$  and, therefore, better reflect  $dT/dE_{EUV}$  of the dayside, where solar EUV control of thermospheric temperature is greater than it is at the terminator.

**Table 1**  
*Correlation Coefficients and Temperature Sensitivities From the Solar and Thermospheric Variability Comparison Shown in Figures 10 and 11*

| LST  | Latitude (°) | $r_{\text{EUV}}$ | $r_{1/R2}$ | $dT/dE_{\text{EUV}}$ (K m <sup>2</sup> /mW) |
|------|--------------|------------------|------------|---|
| Dusk | 50–60        | 0.26             | 0.41       | 26  |
| Dusk | 25–35        | 0.74             | 0.01       | 61  |
| Dusk | –5–5         | 0.71             | 0.7        | 35  |
| Dusk | –65–55       | 0.53             | 0.42       | 32  |
| Dawn | 55–65        | 0.66             | 0.52       | 54  |
| Dawn | 30–40        | 0.4              | 0.54       | 41  |
| Dawn | –15–5        | 0.22             | 0.14       | 16  |
| Dawn | –60–50       | 0.76             | 0.75       | 38  |

## 6. Summary and Conclusions

MAVEN EUVM solar occultations provide a powerful new capability for characterizing the Mars thermosphere and its variability. The channel selected for density retrievals in this study measures wavelengths that are absorbed in the 100–200-km range of the thermosphere. Density retrievals using the other two EUVM channels, which measure irradiance at 0.1–7 and 121.6 nm, can potentially extend this range to lower altitudes because photons in these bands penetrate to lower altitudes due to smaller CO<sub>2</sub> cross sections at these wavelengths. As shown in Figure 4, the retrieval uncertainty becomes large at lower altitudes, primarily due to single scale-height reference atmospheres being used in the retrieval. As

such, multiple scale-height reference atmospheres need to be incorporated into the retrieval method for accurate density retrievals at lower altitudes.

Altitude-latitude maps of thermospheric temperature and density at perihelion and aphelion have been presented, revealing a highly structured and variable thermosphere. Large-scale features are generally consistent with the structure revealed by GCMs, but a more quantitative and direct comparison is needed in order to both gauge and advance the current understanding of processes that determine the structure of the Mars thermosphere. For example, are the high-latitude temperature decreases and density enhancements near aphelion captured in current GCMs? And if not, why? Since gravity wave thermal cooling has been predicted to be substantial at both Earth and Mars (Medvedev & Yiğit, 2012; Yiğit & Medvedev, 2009), yet never directly observed, understanding whether these high-latitude cold features can be attributed to gravity wave cooling is of significant scientific importance for understanding the thermal balance of both Earth's and Mars's thermospheres. Additionally, a close inspection of the perihelion map reveals periodic temperature and density fluctuations. These may be due to nonmigrating tides, but detailed study is needed to understand their origin.

Temperature enhancements from polar warming provide tracers for meridional circulation. Prior limited polar warming observations from accelerometers (Bougher et al., 2006; Bougher, Brain, et al. 2017) and subsequent GCM studies (Bell et al., 2007) have led to a better understanding of the dynamics of the Mars thermosphere. The EUVM-SO observations provide first-ever vertical profiling of polar warming features at intermediate altitudes, which are in remarkable agreement with GCM predictions. Detailed comparisons of this feature with GCM predictions that account for contemporary dust conditions should lead to improved understanding of meridional circulation, and its variability, at Mars.

Observations of the Mars thermosphere response to solar variability at short timescales, and from solar rotations in particular, provide insight into how thermal balance is maintained in the thermosphere. EUVM-SOs observed the thermal response of both the lower and upper thermosphere to two consecutive solar rotations, providing the first observations of the Mars thermosphere's vertical-wind thermostat, which has been predicted to suppress more extreme fluctuations in dayside thermospheric temperatures due to solar EUV heating (Bougher et al., 1999, 2009). These observations, coupled with GCM simulations, should lead to a better understanding of the role of adiabatic and 15- $\mu\text{m}$  cooling in maintaining thermospheric temperatures. For example, can the degree of cooling in the lower thermosphere associated with solar rotations be entirely explained by adiabatically induced vertical winds, or does the resulting increased ionization enhance the relative abundance of atomic O in the lower thermosphere to the extent that 15- $\mu\text{m}$  cooling is enhanced?

A broad range of space weather activity has occurred while MAVEN has been at Mars (Lee et al., 2017). Therefore, the EUVM-SO data set can be used to study the Mars thermosphere response to transient space weather events including solar flares, coronal mass ejections or solar energetic particles. To date, only solar flares have been shown to cause temperature enhancements in the thermosphere (Jain et al., 2018; Thiemann et al., 2015), which have been shown to occur primarily at higher altitudes, be fleeting in nature, and increase the exospheric temperature by up to 50–100 K. The enhancement of EUV irradiance during large flares is comparable to the enhancement occurring over a solar cycle (Woods et al., 2006). It follows, based on the  $dT/dE_{\text{EUV}}$  estimates in section 5.3, that enhancements approaching 123 K could occur near the terminator if we assume these equilibrium estimates apply over the short timescales of flares. The extended altitude range afforded by the EUVM-SO could lead to a better understanding as to why flare-induced temperature

enhancements occur primarily at high altitudes. Indeed, the EUVM-SO observations of the Mars thermosphere response to a solar rotation may provide an important clue into how thermostatic processes dampen the response of the thermosphere to rapid changes in EUV forcing. Further, previous observations of thermospheric flare response have been limited to when MAVEN periapsis has been on the dayside, which excludes a large portion of the MAVEN mission (Thiemann et al., 2015). As such, the addition of the new EUVM-SO measurements increase the statistical likelihood of observing any neutral response to solar flares as well as coronal mass ejections or solar energetic particles.

The EUVM-SO results along with recent results using similar instrumentation and methods at Earth by Thiemann, Dominique, et al. (2017) demonstrate that solar EUV foil filter photometers can effectively characterize a region of planetary thermospheres that has been historically difficult to measure. The simplicity of the instrumentation should be emphasized: The EUVM channel used here consists of a foil filter, limiting aperture, Si diode, and low-current electrometer. These technologies have substantially matured over the past two decades, allowing for foil filter photometers to be built at relatively low cost and small size, with low power and data requirements. As such, they should be considered by mission planners for future planetary mission flights-of-opportunity as either small sun-pointed sensors or separate 2 U sun-pointed CubeSats.

### Acknowledgments

The EUVM data used for deriving solar occultation density retrievals are available at the NASA Planetary Data System (<https://pds.nasa.gov>) in the EUVM Level 2 data product in the "Corrected Counts" variable. Derived temperatures and densities are planned for delivery to the NASA Planetary Data System in 2018. SWAP images used in the density retrievals are publicly available through the SolarSoft IDL package and online at <http://proba2.sidc.be/data/SWAP>. CO<sub>2</sub> cross sections were downloaded from the Max Planck Institute, Mainz UV/Vis Spectral Atlas (Keller-Rudek et al., 2013) at [http://satellite.mpic.de/spectral\\_atlas/index.html](http://satellite.mpic.de/spectral_atlas/index.html). O cross sections (used only in the uncertainty analysis) were downloaded from the Southwest Research Institute PHoto Ionization/Dissociation RATES (PHIDRATES) database at <http://phidrates.space.swri.edu>. The dust opacity maps were downloaded from [http://www-mars.lmd.jussieu.fr/mars/dust\\_climatology/](http://www-mars.lmd.jussieu.fr/mars/dust_climatology/), and the Mars Climate Database outputs were taken from v5.3 of the web interface available at [http://www-mars.lmd.jussieu.fr/mcd\\_python/](http://www-mars.lmd.jussieu.fr/mcd_python/); both websites are hosted by the Laboratoire de Meteorologie Dynamique. E. T., F. G., M. P., L. A., B. T., M. D., S. B., and B. J. were supported by the NASA MAVEN Program. M. D. was supported by the Belgian Federal Science Policy Office through the ESA-PRODEX Program. Z. G. was supported by an appointment to the NASA Postdoctoral Program at NASA Goddard Space Flight Center, administered by Universities Space Research Association under contract with NASA. The authors thank the anonymous reviewer and Roger Yelle for their helpful questions and comments during the peer review process, which have resulted in what we believe to be a better paper. E. T. would like to thank Sonal Jain of the University of Colorado, Boulder; R. Lillis of the University of California, Berkeley; and H. Grollier of the University of Arizona, Tucson, for their helpful conversations on the topic of this study. E. T. also thanks M. West of the Royal Observatory of Belgium for assistance with the PROBA2 SWAP images.

### References

- Arp, U., Friedman, R., Furst, M. L., Makar, S., & Shaw, P. S. (2000). SURF III—An improved storage ring for radiometry. *Metrologia*, *37*(5), 357–360. <https://doi.org/10.1088/0026-1394/37/5/2>
- Bell, J. M., Bougher, S. W., & Murphy, J. R. (2007). Vertical dust mixing and the interannual variations in the Mars thermosphere. *Journal of Geophysical Research*, *112*, E12002. <https://doi.org/10.1029/2006JE002856>
- Bougher, S. W. (1995). Comparative thermospheres: Venus and Mars. *Advances in Space Research*, *15*(4), 21–45. [https://doi.org/10.1016/0273-1177\(94\)00062-6](https://doi.org/10.1016/0273-1177(94)00062-6)
- Bougher, S. W., Bell, J. M., Murphy, J. R., Lopez-Valverde, M. A., & Withers, P. G. (2006). Polar warming in the Mars thermosphere: Seasonal variations owing to changing insolation and dust distributions. *Geophysical Research Letters*, *33*, L02203. <https://doi.org/10.1029/2005GL024059>
- Bougher, S. W., Brain, D. A., Fox, J. L., Gonzalez-Galindo, F., Simon-Wedlund, C., & Withers, P. G. (2017). Chapter 14: Upper atmosphere and ionosphere. In B. Haberle, M. Smith, T. Clancy, F. Forget, & R. Zurek (Eds.), *The atmosphere and climate of Mars* (Chap. 14, 433 pp.). Cambridge, UK: Cambridge University Press. <https://doi.org/10.1017/9781107016187>
- Bougher, S. W., Cravens, T. E., Grebowsky, J., & Luhmann, J. (2015). The aeronomy of Mars: Characterization by MAVEN of the upper atmosphere reservoir that regulates volatile escape. *Space Science Reviews*, *195*(1–4), 423–456. <https://doi.org/10.1007/s11214-014-0053-7>
- Bougher, S. W., Engel, S., Roble, R. G., & Foster, B. (1999). Comparative terrestrial planet thermospheres: 2. Solar cycle variation of global structure and winds at equinox. *Journal of Geophysical Research*, *104*(E7), 16,591–16,611. <https://doi.org/10.1029/1998JE001019>
- Bougher, S. W., Engel, S., Roble, R. G., & Foster, B. (2000). Comparative terrestrial planet thermospheres: 3. Solar cycle variation of global structure and winds at solstices. *Journal of Geophysical Research*, *105*(E7), 17,669–17,692. <https://doi.org/10.1029/1999JE001232>
- Bougher, S. W., Jakosky, B., Halekas, J., Grebowsky, J., Luhmann, J., Mahaffy, P., et al. (2015). Early MAVEN Deep Dip campaign reveals thermosphere and ionosphere variability. *Science*, *350*(6261), aad0459.
- Bougher, S. W., McDunn, T. M., Zoldak, K. A., & Forbes, J. M. (2009). Solar cycle variability of Mars dayside exospheric temperatures: Model evaluation of underlying thermal balances. *Geophysical Research Letters*, *36*, L05201. <https://doi.org/10.1029/2008GL036376>
- Bougher, S. W., Pawlowski, D., Bell, J. M., Nelli, S., McDunn, T., Murphy, J. R., et al. (2015). Mars global ionosphere-thermosphere model: Solar cycle, seasonal, and diurnal variations of the Mars upper atmosphere. *Journal of Geophysical Research: Planets*, *120*, 311–342. <https://doi.org/10.1002/2014JE004715>
- Bougher, S. W., Roble, R. G., & Fuller-Rowell, T. (2002). Simulations of the upper atmospheres of the terrestrial planets. In *Atmospheres in the solar system: Comparative aeronomy* (pp. 261–288). Washington, D.C.: American Geophysical Union.
- Bougher, S. W., Roeten, K., Olsen, K., Mahaffy, P. R., Benna, M., Elrod, M., et al. (2017). The structure and variability of Mars dayside thermosphere from MAVEN NGIMS and IUVS measurements: Seasonal and solar activity trends in scale heights and temperatures. *Journal of Geophysical Research: Space Physics*, *122*, 1296–1313. <https://doi.org/10.1002/2016JA023454>
- Elrod, M. K., Bougher, S., Bell, J., Mahaffy, P. R., Benna, M., Stone, S., et al. (2017). He bulge revealed: He and CO<sub>2</sub> diurnal and seasonal variations in the upper atmosphere of Mars as detected by MAVEN NGIMS. *Journal of Geophysical Research: Space Physics*, *122*, 2564–2573. <https://doi.org/10.1002/2016JA023482>
- Eparvier, F. G., Chamberlin, P. C., Woods, T. N., & Thiemann, E. M. B. (2015). The solar extreme ultraviolet monitor for MAVEN. *Space Science Reviews*, *195*(1–4), 293–301. <https://doi.org/10.1007/s11214-015-0195-2>
- Evans, J. S., Stevens, M. H., Lumpe, J. D., Schneider, N. M., Stewart, A. I. F., Deighan, J., et al. (2015). Retrieval of CO<sub>2</sub> and N<sub>2</sub> in the Martian thermosphere using dayglow observations by IUVS on MAVEN. *Geophysical Research Letters*, *42*, 9040–9049. <https://doi.org/10.1002/2015GL065489>
- Fjeldbo, G., Fjeldbo, W. C., & Eshleman, V. R. (1966). Models for the atmosphere of Mars based on the Mariner 4 occultation experiment. *Journal of Geophysical Research*, *71*(9), 2307–2316. <https://doi.org/10.1029/JZ071i009p02307>
- Forbes, J. M., Bruinsma, S., & Lemoine, F. G. (2006). Solar rotation effects on the thermospheres of Mars and Earth. *Science*, *312*(5778), 1366–1368. <https://doi.org/10.1126/science.1126389>
- Forget, F., Hourdin, F., Fournier, R., Hourdin, C., Talagrand, O., Collins, M., et al. (1999). Improved general circulation models of the Martian atmosphere from the surface to above 80 km. *Journal of Geophysical Research*, *104*(E10), 24,155–24,175. <https://doi.org/10.1029/1999JE001025>
- Gallagher, J. W., Brion, C. E., Samson, J. A. R., & Langhoff, P. W. (1988). Absolute cross sections for molecular photoabsorption, partial photoionization, and ionic photofragmentation processes. *Journal of Physical and Chemical Reference Data*, *17*(1), 9–153. <https://doi.org/10.1063/1.555821>

- González-Galindo, F., Forget, F., López-Valverde, M. A., & Angelats i Coll, M. (2009). A ground-to-exosphere Martian general circulation model: 2. Atmosphere during solstice conditions—Thermospheric polar warming. *Journal of Geophysical Research*, *114*, E08004. <https://doi.org/10.1029/2008JE003277>
- González-Galindo, F., Forget, F., López-Valverde, M. A., Angelats i Coll, M., & Millour, E. (2009). A ground-to-exosphere Martian general circulation model: 1. Seasonal, diurnal, and solar cycle variation of thermospheric temperatures. *Journal of Geophysical Research*, *114*, E08004. <https://doi.org/10.1029/2008JE003277>
- González-Galindo, F., López-Valverde, M. A., Angelats i Coll, M., & Forget, F. (2005). Extension of a Martian general circulation model to thermospheric altitudes: UV heating and photochemical models. *Journal of Geophysical Research*, *110*, E09008. <https://doi.org/10.1029/2004JE002312>
- González-Galindo, F., López-Valverde, M. A., Forget, F., García-Comas, M., Millour, E., & Montabone, L. (2015). Variability of the Martian thermosphere during eight Martian years as simulated by a ground-to-exosphere global circulation model. *Journal of Geophysical Research: Planets*, *120*, 2020–2035. <https://doi.org/10.1002/2015JE004925>
- Gröller, H., Montmessin, F., Yelle, R. V., Lefèvre, F., Forget, F., Schneider, N. M., et al. (2018). MAVEN/IUVS stellar occultation measurements of Mars atmospheric structure and composition. *Journal of Geophysical Research: Planets*, *123*, 1449–1483. <https://doi.org/10.1029/2017JE005466>
- Gröller, H., Yelle, R. V., Koskinen, T. T., Montmessin, F., Lacombe, G., Schneider, N. M., et al. (2015). Probing the Martian atmosphere with MAVEN/IUVS stellar occultations. *Geophysical Research Letters*, *42*, 9064–9070. <https://doi.org/10.1002/2015GL065294>
- Gullikson, E. M., Korde, R., Canfield, L. R., & Vest, R. E. (1996). Stable silicon photodiodes for absolute intensity measurements in the VUV and soft X-ray regions. *Journal of Electron Spectroscopy and Related Phenomena*, *80*, 313–316. [https://doi.org/10.1016/0368-2048\(96\)02983-0](https://doi.org/10.1016/0368-2048(96)02983-0)
- Huebner, W. F., & Mukherjee, J. (2015). Photoionization and photodissociation rates in solar and blackbody radiation fields. *Planetary and Space Science*, *106*, 11–45. <https://doi.org/10.1016/j.pss.2014.11.022>
- Huestis, D. L., & Berkowitz, J. (2011). Critical evaluation of the photoabsorption cross section of CO<sub>2</sub> from 0.125 to 201.6 nm at room temperature. *Planetary Science, Advances in Geosciences*, *25*, 229–242.
- Jain, S. K., Deighan, J., Schneider, N. M., Stewart, A. I. F., Evans, J. S., Thiemann, E. M. B., et al. (2018). Martian thermospheric response to an X8.2 Solar Flare on September 10, 2017 as seen by MAVEN/IUVS. *Geophysical Research Letters*, *45*. <https://doi.org/10.1029/2018GL077731>
- Jain, S. K., Stewart, A. I. F., Schneider, N. M., Deighan, J., Stiepen, A., Evans, J. S., et al. (2015). The structure and variability of Mars upper atmosphere as seen in MAVEN/IUVS dayglow observations. *Geophysical Research Letters*, *42*, 9023–9030. <https://doi.org/10.1002/2015GL065419>
- Jakosky, B. M., Lin, R. P., Grebowsky, J. M., Luhmann, J. G., Mitchell, D. F., Beutelschies, G., et al. (2015). The Mars atmosphere and volatile evolution (MAVEN) mission. *Space Science Reviews*, *195*(1–4), 3–48. <https://doi.org/10.1007/s11214-015-0139-x>
- Keating, G. M., Bougher, S. W., Zurek, R. W., Tolson, R. H., Cancro, G. J., Noll, S. N., et al. (1998). The structure of the upper atmosphere of Mars: In situ accelerometer measurements from Mars Global Surveyor. *Science*, *279*(5357), 1672–1676. <https://doi.org/10.1126/science.279.5357.1672>
- Keller-Rudek, H., Moortgat, G. K., Sander, R., & Sörensen, R. (2013). The MPI-Mainz UV/VIS spectral atlas of gaseous molecules of atmospheric interest. *Earth System Science Data*, *5*(2), 365–373. <https://doi.org/10.5194/essd-5-365-2013>
- Lee, C. O., Hara, T., Halekas, J. S., Thiemann, E., Chamberlin, P., Eparvier, F., et al. (2017). MAVEN observations of the solar cycle 24 space weather conditions at Mars. *Journal of Geophysical Research: Space Physics*, *122*, 2768–2794. <https://doi.org/10.1002/2016JA023495>
- Liu, G., England, S., Lillis, R. J., Mahaffy, P. R., Elrod, M., Benna, M., & Jakosky, B. (2017). Longitudinal structures in Mars' upper atmosphere as observed by MAVEN/NGIMS. *Journal of Geophysical Research: Space Physics*, *122*, 1258–1268. <https://doi.org/10.1002/2016JA023455>
- Lo, D. Y., Yelle, R. V., Schneider, N. M., Jain, S. K., Stewart, A. I. F., England, S. L., et al. (2015). Nonmigrating tides in the Martian atmosphere as observed by MAVEN IUVS. *Geophysical Research Letters*, *42*, 9057–9063. <https://doi.org/10.1002/2015GL066268>
- Madeleine, J. B., Forget, F., Millour, E., Montabone, L., & Wolff, M. J. (2011). Revisiting the radiative impact of dust on Mars using the LMD global climate model. *Journal of Geophysical Research: Planets*, *116*, E11010. <https://doi.org/10.1029/2011JE003855>
- Mahaffy, P. R., Benna, M., Elrod, M., Yelle, R. V., Bougher, S. W., Stone, S. W., & Jakosky, B. M. (2015). Structure and composition of the neutral upper atmosphere of Mars from the MAVEN NGIMS investigation. *Geophysical Research Letters*, *42*, 8951–8957. <https://doi.org/10.1002/2015GL065329>
- Mahaffy, P. R., Benna, M., King, T., Harpold, D. N., Arvey, R., Barciniak, M., et al. (2015). The neutral gas and ion mass spectrometer on the Mars atmosphere and volatile evolution mission. *Space Science Reviews*, *195*(1–4), 49–73. <https://doi.org/10.1007/s11214-014-0091-1>
- McClintock, W. E., Schneider, N. M., Holsclaw, G. M., Clarke, J. T., Hoskins, A. C., Stewart, I., et al. (2015). The imaging ultraviolet spectrograph (IUVS) for the MAVEN mission. *Space Science Reviews*, *195*(1–4), 75–124. <https://doi.org/10.1007/s11214-014-0098-7>
- Medvedev, A. S., González-Galindo, F., Yiğit, E., Feofilov, A. G., Forget, F., & Hartogh, P. (2015). Cooling of the Martian thermosphere by CO<sub>2</sub> radiation and gravity waves: An intercomparison study with two general circulation models. *Journal of Geophysical Research: Planets*, *120*, 913–927. <https://doi.org/10.1002/2015JE004802>
- Medvedev, A. S., & Yiğit, E. (2012). Thermal effects of internal gravity waves in the Martian upper atmosphere. *Geophysical Research Letters*, *39*, L05201. <https://doi.org/10.1029/2012GL050852>
- Medvedev, A. S., Yiğit, E., Hartogh, P., & Becker, E. (2011). Influence of gravity waves on the Martian atmosphere: General circulation modeling. *Journal of Geophysical Research*, *116*, E10004. <https://doi.org/10.1029/2011JE003848>
- Millour, E., Forget, F., Spiga, A., Navarro, T., Madeleine, J. B., Montabone, L., et al. (2015, September). The Mars Climate Database (MCD version 5.2). In *European Planetary Science Congress 2015* (Vol. 10, pp. EPSC2015–438). EPSC.
- Montabone, L., Forget, F., Millour, E., Wilson, R. J., Lewis, S. R., Cantor, B., et al. (2015). Eight-year climatology of dust optical depth on Mars. *Icarus*, *251*, 65–95. <https://doi.org/10.1016/j.icarus.2014.12.034>
- Nier, A. O., & McElroy, M. B. (1977). Composition and structure of Mars' upper atmosphere: Results from the neutral mass spectrometers on Viking 1 and 2. *Journal of Geophysical Research*, *82*(28), 4341–4349. <https://doi.org/10.1029/J5082i028p04341>
- Picone, J. M., Hedin, A. E., Drob, D. P., & Aikin, A. C. (2002). NRLMSISE-00 empirical model of the atmosphere: Statistical comparisons and scientific issues. *Journal of Geophysical Research*, *107*(A12), 1468. <https://doi.org/10.1029/2002JA009430>
- Powell, F. R. (1993). Care and feeding of soft X-ray and extreme ultraviolet filters. In *24th Annual Boulder Damage Symposium Proceedings—Laser-induced damage in optical materials: 1992* (Vol. 1848, pp. 503–516). Bellingham, WA: International Society for Optics and Photonics.
- Roble, R. G., & Norton, R. B. (1972). Thermospheric molecular oxygen from solar extreme-ultraviolet occultation measurements. *Journal of Geophysical Research*, *77*(19), 3524–3533.
- Seaton, D. B., Berghmans, D., Nicula, B., Halain, J. P., De Groof, A., Thibert, T., et al. (2013). The SWAP EUV imaging telescope part I: Instrument overview and pre-flight testing. *Solar Physics*, *286*(1), 43–65. <https://doi.org/10.1007/s11207-012-0114-6>

- Snowden, D., Yelle, R. V., Cui, J., Wahlund, J. E., Edberg, N. J. T., & Ågren, K. (2013). The thermal structure of Titan's upper atmosphere, I: Temperature profiles from Cassini INMS observations. *Icarus*, *226*(1), 552–582. <https://doi.org/10.1016/j.icarus.2013.06.006>
- Terada, N., Leblanc, F., Nakagawa, H., Medvedev, A. S., Yiğit, E., Kuroda, T., et al. (2017). Global distribution and parameter dependences of gravity wave activity in the Martian upper thermosphere derived from MAVEN/NGIMS observations. *Journal of Geophysical Research: Space Physics*, *122*, 2374–2397. <https://doi.org/10.1002/2016JA023476>
- Thiemann, E. M. (2016). Multi-spectral sensor driven solar EUV irradiance models with improved spectro-temporal resolution for space weather applications at Earth and Mars (Doctoral Dissertation, University of Colorado at Boulder).
- Thiemann, E. M. B., Chamberlin, P. C., Eparvier, F. G., Templeman, B., Woods, T. N., Bougher, S. W., & Jakosky, B. M. (2017). The MAVEN EUVM model of solar spectral irradiance variability at Mars: Algorithms and results. *Journal of Geophysical Research: Space Physics*, *122*, 2748–2767. <https://doi.org/10.1002/2016JA023512>
- Thiemann, E. M. B., Dominique, M., Pilinski, M. D., & Eparvier, F. G. (2017). Vertical Thermospheric density profiles from EUV solar occultations made by PROBA2 LYRA for solar cycle 24. *Space Weather*, *15*, 1649–1660. <https://doi.org/10.1002/2017SW001719>
- Thiemann, E. M. B., Eparvier, F. G., Andersson, L. A., Fowler, C. M., Peterson, W. K., Mahaffy, P. R., et al. (2015). Neutral density response to solar flares at Mars. *Geophysical Research Letters*, *42*, 8986–8992. <https://doi.org/10.1002/2015GL066334>
- Thiemann, E. M. B., Eparvier, F. G., & Woods, T. N. (2017). A time dependent relation between EUV solar flare light-curves from lines with differing formation temperatures. *Journal of Space Weather and Space Climate*, *7*, A36. <https://doi.org/10.1051/swsc/2017037>
- Vadas, S. L., Liu, H. L., & Lieberman, R. S. (2014). Numerical modeling of the global changes to the thermosphere and ionosphere from the dissipation of gravity waves from deep convection. *Journal of Geophysical Research: Space Physics*, *119*, 7762–7793. <https://doi.org/10.1002/2014JA020280>
- Withers, P. (2006). Mars global surveyor and Mars odyssey accelerometer observations of the Martian upper atmosphere during aerobraking. *Geophysical Research Letters*, *33*, L02201. <https://doi.org/10.1029/2005GL024447>
- Woods, T. N., Hock, R., Eparvier, F., Jones, A. R., Chamberlin, P. C., Klimchuk, J. A., et al. (2011). New solar extreme-ultraviolet irradiance observations during flares. *The Astrophysical Journal*, *739*(2), 59. <https://doi.org/10.1088/0004-637X/739/2/59>
- Woods, T. N., Kopp, G., & Chamberlin, P. C. (2006). Contributions of the solar ultraviolet irradiance to the total solar irradiance during large flares. *Journal of Geophysical Research*, *111*, A10S14. <https://doi.org/10.1029/2005JA011507>
- Woods, T. N., Rodgers, E., Bailey, S. M., Eparvier, F. G., & Ucker, G. (1999). TIMED solar EUV experiment: Pre-flight calibration results for the XUV photometer system. In *Proceedings of SPIE—The International Society for Optical Engineering* (Vol. 3756, pp. 255–264). Denver, CO: SPIE.
- Woods, T. N., Rottman, G., & Vest, R. (2005). XUV photometer system (XPS): Overview and calibrations. *The Solar Radiation and Climate Experiment (SORCE)*, 345–374. [https://doi.org/10.1007/0-387-37625-9\\_16](https://doi.org/10.1007/0-387-37625-9_16)
- Yiğit, E., England, S. L., Liu, G., Medvedev, A. S., Mahaffy, P. R., Kuroda, T., & Jakosky, B. M. (2015). High-altitude gravity waves in the Martian thermosphere observed by MAVEN/NGIMS and modeled by a gravity wave scheme. *Geophysical Research Letters*, *42*, 8993–9000. <https://doi.org/10.1002/2015GL065307>
- Yiğit, E., & Medvedev, A. S. (2009). Heating and cooling of the thermosphere by internal gravity waves. *Geophysical Research Letters*, *36*, L14807. <https://doi.org/10.1029/2009GL038507>
- Yiğit, E., Medvedev, A. S., & Hartogh, P. (2015). Gravity waves and high-altitude CO<sub>2</sub> ice cloud formation in the Martian atmosphere. *Geophysical Research Letters*, *42*, 4294–4300. <https://doi.org/10.1002/2015GL064275>
- Zurek, R. W., Tolson, R. A., Bougher, S. W., Lugo, R. A., Baird, D. T., Bell, J. M., & Jakosky, B. M. (2017). Mars thermosphere as seen in MAVEN accelerometer data. *Journal of Geophysical Research: Space Physics*, *122*, 3798–3814. <https://doi.org/10.1002/2016JA023641>
- Zurek, R. W., Tolson, R. H., Baird, D., Johnson, M. Z., & Bougher, S. W. (2015). Application of MAVEN accelerometer and attitude control data to Mars atmospheric characterization. *Space Science Reviews*, *195*(1–4), 303–317. <https://doi.org/10.1007/s11214-014-0095-x>